

2

SRI International

AD-A268 849



Quarterly Technical Report 4 • 24 August 1993

IR MATERIALS PRODUCIBILITY

A. Sher, Program Director
M.A. Berding, Sr. Research Physicist
A.T. Paxton, Research Physicist
Physical Electronics Laboratory
M.W. Muller, Consultant

SRI Project 3820

Prepared for:

Contracting Officers Technical Representative
Defense Advanced Research Projects Agency
Microelectronics Technology Office (MTO)
3701 N. Fairfax Drive
Arlington, VA 22203-1714

Attn: Mr. Raymond Balcerak

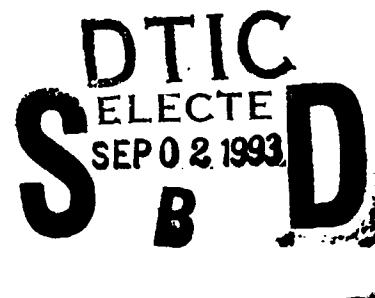
ARPA Order No. 8557; Program Code Nos. 2H20, 2D10

Contract MDA972-92-C-0053

Covering the period: 1 May through 31 July 1993

The views and conclusions contained in this document are those of the authors and should not be interpreted as representing the official policies, either expressed or implied, of the Advanced Research Projects Agency or the U.S. Government.

APPROVED FOR PUBLIC RELEASE
DISTRIBUTION UNLIMITED



93-20494 4508

IR MATERIALS PRODUCIBILITY

A. Sher, Program Director
M.A. Berding, Sr. Research Physicist
A.T. Paxton, Research Physicist
Physical Electronics Laboratory
M.W. Muller, Consultant

SRI Project 3820

Prepared for:

Contracting Officers Technical Representative
Defense Advanced Research Projects Agency
Microelectronics Technology Office (MTO)
3701 N. Fairfax Drive
Arlington, VA 22203-1714
Attn: Mr. Raymond Balcerak

ARPA Order No. 8557; Program Code Nos. 2H20, 2D10

Contract MDA972-92-C-0053

Covering the period: 1 May through 31 July 1993

The views and conclusions contained in this document are those of the authors and should not be interpreted as representing the official policies, either expressed or implied, of the Advanced Research Projects Agency or the U.S. Government.

APPROVED FOR PUBLIC RELEASE
DISTRIBUTION UNLIMITED

Approved:

Eric Pearson, Director
Physical Electronics Laboratory

Donald L. Nielson, Vice President
Computing and Engineering Sciences Division

REPORT DOCUMENTATION PAGE			Form Approved OMB No. 0704-0188	
Public reporting burden for this collection of information is estimated to average 1 hour per response, including the time for reviewing instructions, searching existing data sources, gathering and maintaining the data needed, and completing and reviewing the collection of information. Send comments regarding this burden estimate or any other aspect of this collection of information, including suggestions for reducing this burden, to Washington Headquarters Services, Directorate for Information Operations and Reports, 1215 Jefferson Davis Highway, Suite 1204, Arlington, VA 22202-4302, and to the Office of Management and Budget, Paperwork Reduction Project (0704-0188), Washington, DC 20503.				
1. AGENCY USE ONLY (Leave Blank)	2. REPORT DATE August 1993	3. REPORT TYPE AND DATES COVERED Quarterly Tech. Rpt. 4, 5-1-93 to 7-31-93		
4. TITLE AND SUBTITLE IR Materials Producibility		5. FUNDING NUMBERS		
6. AUTHORS A. Sher, M.A. Berding, A.T. Paxton, SRI International M. Muller, Consultant				
7. PERFORMING ORGANIZATION NAME(S) AND ADDRESS(ES) SRI International 333 Ravenswood Avenue Menlo Park, CA 94025-3493		8. PERFORMING ORGANIZATION REPORT NUMBER		
9. SPONSORING/MONITORING AGENCY NAME(S) AND ADDRESS(ES) Defense Advanced Research Projects Agency Microelectronics Technology Office (MTO), Infrared Focal Plane Array Program 3701 N. Fairfax Drive Arlington, VA 22203-1714		10. SPONSORING/MONITORING AGENCY REPORT NUMBER		
11. SUPPLEMENTARY NOTES				
12a. DISTRIBUTION/AVAILABILITY STATEMENT Approved for public release; distribution unlimited		12b. DISTRIBUTION CODE		
13. ABSTRACT (Maximum 200 words) During this quarter, we completed an important component of our work on the gradient corrections to the defect formation energies. This correction applies to all total energies calculated, including those for defects in HgCeTe, ZnSe, and LiNbO ₃ , and permits us to calculate accurate absolute defect densities. We have developed a preliminary description of the tellurium inclusion formation process in HgCdTe, and proposed a mechanism for the mobility reduction in undoped mercury-annealed LPE material. We have begun the calculation of the lithium vacancy formation energies in LiNbO ₃ . We have continued our work on the impact of dislocations on MCT device properties. We have calculated the electron mobility in Hg _{0.22} Cd _{0.78} Te by solving the Boltzmann transport equation with Fermi-Dirac statistics and the full band structure, and have obtained excellent agreement with experiments. The transport-related properties (Hall coefficient, Fermi level, and energy gap) have also been calculated with accurate analytical band structures and Fermi-Dirac statistics, and we find that the results differ appreciably from those using traditional approximations. All of these results are being incorporated into processing strategies to increase yields and performance of devices.				
14. SUBJECT TERMS native point defect; defect density; photonic material; IRFPA; HgTe; CdTe; ZnSe; HgCdTe; LiNbO ₃ ; dislocation; Boltzmann transport equation		15. NUMBER OF PAGES 56		
		16. PRICE CODE		
17. SECURITY CLASSIFICATION OF REPORT Unclassified	18. SECURITY CLASSIFICATION OF THIS PAGE Unclassified	19. SECURITY CLASSIFICATION OF ABSTRACT Unclassified	20. LIMITATION OF ABSTRACT Unlimited	

SUMMARY

The work summarized in this report covers the fourth quarter of a program with a goal that is twofold: first, to study the properties of native point defect in infrared focal-plan array (IRFPA) active and substrate materials, and second, to study the properties of native point defects in two classes of photonic materials, the wide-gap II-VI compounds (ZnSe as the prototype for which impurity properties will also be calculated) and the nonlinear optical materials (LiNbO₃ as the prototype). Our accomplishments in the fourth quarter include

- Completion of a study of the gradient correction to the local density approximation, which is an essential ingredient to our calculations of accurate absolute defect concentrations in HgCdTe, ZnSe, and LiNbO₃.
- Calculation of the degeneracy factors for the the single and double donor and acceptor states of the native defects.
- Analysis of strategies for calculating the localized states in ZnSe.
- Development of a preliminary description of the tellurium inclusion formation process and their native point defect atmospheres in HgCdTe, and proposal of a mechanism for the mobility reduction in mercury-annealed liquid phase epitaxy (LPE) material.
- Development of input for defect calculations in LiNbO₃, and beginning of calculation of the lithium vacancy formation energy in LiNbO₃.
- Calculation of the electron mobility in Hg_{0.22}Cd_{0.78}Te from a solution of the full Boltzmann transport equation with Fermi-Dirac statistics and an accurate band structure. Excellent agreement with experiments has been obtained
- Calculation of transport-related properties (Hall coefficient, Fermi level, and energy gap) using accurate band structures and Fermi-Dirac statistics. Results differ appreciably from those using traditional approximations.

DTIC QUALITY INSPECTED 2

Accession For	
NTIS GRA&I	<input checked="checked" type="checkbox"/>
DTIC TAB	<input type="checkbox"/>
Unannounced	<input type="checkbox"/>
Justification	
By _____	
Distribution/	
Availability Codes	
Dist	Avail and/or Special
A-1	

CONTENTS

1.	NATIVE POINT DEFECTS IN HgCdTe, ZnSe, AND LiNbO₃	1
1.1	Gradient Correction to the Local Density Formalism.....	1
1.2	Degeneracy Factors for Donor and Acceptor Levels	6
1.3	Tellurium Inclusion in MCT	6
2.	DISLOCATIONS IN MCT	7
3.	TRANSPORT PROPERTIES OF HgCdTe	7
4.	WIDE-GAP II-VI COMPOUNDS (ZnSe AS PROTOTYPE).....	8
5.	NONLINEAR OPTICAL MATERIALS (LiNbO₃ AS THE PROTOTYPE)	8
6.	WORK PLANNED	9
	REFERENCES	11
	APPENDICES	
A.	Dislocations and Junction Performance in MCT	A-1
B.	Transport Studies in Narrow-Gap Semiconductors Revisited	B-1

1. NATIVE POINT DEFECTS IN HgCdTe, ZnSe AND LiNbO₃

1.1 GRADIENT CORRECTION TO THE LOCAL DENSITY FORMALISM

During this quarter, we completed an important component of our work on defects in HgCdTe, ZnSe, and LiNbO₃, which is the gradient correction¹ to the local density (LD) formalism. The gradient correction (GC) is important in giving our theoretical numbers the accuracy necessary to calculate absolute defect concentrations, a task that to our knowledge no others have attempted to date.

Although we have been using the gradient correction for some time, a recent paper in the literature² has raised some issues about the systematics of the correction. We have thus felt it necessary to undertake a more careful analysis of the gradient correction, both to address the issues raised by the paper's authors, for our own understanding, and to establish the reliability of our defect work, which will include the correction.

In Tables 1 through 4 we show the results of our study of the gradient correction on the lattice constant, bond energy, bulk modulus, and $c_{11}-c_{12}$ elastic constant, respectively. Shown in these tables are the results for the diamond and zincblende semiconductors. Below we discuss in turn the results in each table.

As can be seen from Table 1, the lattice constants calculated with the LD and GC are both in good agreement with the experimental results. The GC consistently lengthens the lattice constant with respect to the LD; in some cases this improves the agreement with experiment, in others it worsens the agreement. In both cases the average agreement with experiment of this *ab initio* theory is better than < 1%, which is quite remarkable.

The bond energy is defined as the magnitude of the crystal energy, per bond, relative to the free atom energies of the constituents. For example the bond energy, E_B for ZnSe is defined via:



The bond energy is multiplied by four in this reaction because four ZnSe bonds are broken in the reaction. With one exception (InP), the agreement of the bond energy with the experimental values is improved significantly when the gradient correction is included in the calculation. In all cases the LD overestimates the binding in the semiconductors - that is, the cohesive energies are too large. The GC bond energies are reduced with respect to the LD; in some cases this results in a slight underbinding. If we consider HgTe (the primary constituent of low x Hg_{1-x}Cd_xTe and ZnSe), the improvement in the bond energies is dramatic: for HgTe we go from a 35% overbinding in LD to only a 6% underbinding with the GC. For ZnSe, the LD predicts a bond energy that is 27% too large, while the GC predicts only a 5% overbinding. Because we are interested in calculating total energies in which the free atom is the reference state, for example the formation of a Zn vacancy via the reaction

Table 1. Comparison of lattice constant, in atomic units, for various zincblende semiconductors using the local density (LD) approximation and the gradient correction (GC) to the local density. Shown for comparison are the experimental values. Values shown in parentheses are the percentage difference from the experimental values.

Compound	Experiment	LD	GC
Si	10.27	10.21(-1%)	10.28(< 1%)
Ge	10.69	10.65(< 1%)	10.74(< 1%)
AlP	10.33	10.27(-1%)	10.36(< 1%)
AlAs	10.70	10.65(< 1%)	10.73(< 1%)
AlSb	11.60	11.57(< 1%)	11.68(+1%)
GaP	10.30	10.21(-1%)	10.30(< 1%)
GaAs	10.69	10.63(-1%)	10.73(< 1%)
GaSb	11.50	11.50(< 1%)	11.62(+1%)
InP	11.09	11.03(-1%)	11.13(< 1%)
InAs	11.45	11.43(< 1%)	11.54(+1%)
InSb	12.25	12.25(< 1%)	12.38(+1%)
ZnS	10.23	10.02(-2%)	10.16(-1%)
ZnSe	10.71	10.55(-1%)	10.68(< 1%)
ZnTe	11.53	11.38(-1%)	11.51(< 1%)
CdS	11.00	10.89(-1%)	11.03(< 1%)
CdSe	11.44	11.38(-1%)	11.53(+1%)
CdTe	12.25	12.16(-1%)	12.32(+1%)
HgS	11.06	10.94(-1%)	11.09(< 1%)
HgSe	11.50	11.46(< 1%)	11.60(+1%)
HgTe	12.21	12.20(< 1%)	12.33(+1%)

Table 2. Comparison of bond energy, in electron volts, for various zincblende semi-conductors using the local density (LD) approximation and the gradient correction (GC) to the local density. Shown for comparison are the experimental values. Values shown in parentheses are the percentage difference from the experimental values.

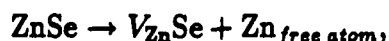
Compound	Experiment	LD	GC
Si	2.32	2.58(+11%)	2.31(< 1%)
Ge	1.94	2.22(+14%)	1.88(-3%)
AlP	2.13	2.35(+10%)	2.05(-4%)
AlAs	1.89	2.17(+15%)	1.85(-2%)
AlSb	1.76	1.91(+9%)	1.61(-9%)
GaP	1.78	2.08(+17%)	1.76(-1%)
GaAs	1.63	1.91(+17%)	1.56(-4%)
GaSb	1.48	1.70(+15%)	1.36(-8%)
InP	1.74	1.89(+9%)	1.56(-10%)
InAs	1.55	1.77(+14%)	1.42(-8%)
InSb	1.40	1.60(+14%)	1.26(-10%)
ZnS	1.59	1.82(+14%)	1.53(-4%)
ZnSe	1.29	1.64(+27%)	1.35(+5%)
ZnTe	1.20	1.43(+19%)	1.15(-4%)
CdS	1.42	1.63(+15%)	1.33(-6%)
CdSe	1.21	1.49(+23%)	1.19(-2%)
CdTe	1.10	1.33(+21%)	1.04(-5%)
HgS	1.02	1.29(+26%)	0.94(-8%)
HgSe	0.85	1.19(+40%)	0.84(-1%)
HgTe	0.81	1.09(+35%)	0.76(-6%)

Table 3. Comparison of bulk modulus, in units of 10^{11} ergs/cm³, for various zincblende semiconductors using the local density (LD) approximation and the gradient correction (GC) to the local density. Shown for comparison are the experimental values. Values shown in parentheses are the percentage difference from the experimental values.

Compound	Experiment	LD	GC
Si	9.92	9.61(-3%)	9.32(-6%)
Ge	7.65	7.13(-7%)	6.77(-11%)
AlSb	5.82	5.58(-4%)	5.32(-9%)
GaP	9.14	8.94(-2%)	8.50(-7%)
GaAs	7.84	7.30(-7%)	6.86(-12%)
GaSb	5.79	5.38(-7%)	4.97(-14%)
InP	7.25	7.01(-3%)	6.61(-9%)
InAs	5.79	5.92(+2%)	5.52(-5%)
InSb	4.82	4.59(-5%)	4.22(-12%)
ZnS	7.64	8.57(+12%)	7.87(+3%)
ZnSe	6.46	7.13(+10%)	6.42(-1%)
ZnTe	5.28	5.49(+4%)	4.98(-6%)
CdTe	4.21	4.58(+9%)	4.05(-4%)
HgS	6.86	7.41(+8%)	5.85(-15%)
HgSe	4.97	5.77(+16%)	5.11(+3%)
HgTe	4.23	4.64(+6%)	4.49(-1%)

Table 4. Comparison of $c_{11}-c_{12}$, in units of 10^{11} ergs/cm³, for various zincblende semiconductors using the local density (LD) approximation and the gradient correction (GC) to the local density. Shown for comparison are the experimental values. Values shown in parentheses are the percentage difference from the experimental values.

Compound	Experiment	LD	GC
Si	10.27	10.26(0%)	9.83(-4%)
Ge	8.19	7.84(-4%)	7.47(-9%)
AlSb	4.43	4.64(+5%)	4.42(0%)
GaP	7.87	8.14(+3%)	7.70(-2%)
GaAs	6.55	6.42(-2%)	6.07(-7%)
GaSb	4.95	4.69(-5%)	4.46(-10%)
InP	4.46	4.63(+4%)	4.45(+0%)
InAs	3.80	3.86(+2%)	3.68(-3%)
InSb	4.82	2.99(-38%)	2.96(-39%)
ZnS	3.54	4.40(+24%)	4.40(+24%)
ZnSe	3.56	3.78(+6%)	3.80(+7%)
ZnTe	3.06	3.67(+20%)	3.42(+12%)
CdTe	1.68	2.06(+23%)	2.01(+20%)
HgS	1.91	1.63(-15%)	1.65(-14%)
HgSe	1.70	1.49(-12%)	1.62(-5%)
HgTe	1.82	1.80(-1%)	1.81(-1%)



it is this feature of the GC in which we are most interested. It appears that the GC is most important not in the calculation of the energy of the solid, but rather in the energy of the free atom. Our work on other elemental solids in the periodic table – for example solid antimony, aluminum, zinc, and tellurium – will allow us to substantiate this observation. The work on the gradient correction has also been supported by ONR contract N00014-91-C-0139. Although the majority of the computations we plan to do to test the gradient correction have been completed, we expect to complete our analysis and interpretation of the results in the next quarter.

1.2 DEGENERACY FACTORS FOR DONOR AND ACCEPTOR LEVELS

One of the ingredients that enters into the calculation of the defect densities is the degeneracy of the particular ionization state of the defect. While the formulas for these degeneracies are well established for the shallow-level impurities with a single ionization state, the degeneracies of the deep state, such as those that arise from the localized potentials of the native defects, have not been worked out. We have completed an analysis of the degeneracies for the states for the various donor and acceptor levels of the vacancies, antisites, and interstitials in the zincblende semiconductors, and incorporated our results into our codes for calculating the defect densities. The details of this analysis will be included in a long paper under preparation for publication.

1.3 TELLURIUM INCLUSION IN MCT

We have begun to investigate the formation of tellurium inclusions and their relationship to the mercury vacancy and tellurium antisite densities in HgCdTe. In the analysis, we have used our results on the defect concentrations in HgCdTe as well as some of the literature on self-diffusion in HgCdTe. Although this problem necessitates more information about diffusion than is currently available, we have used available information to construct a description of the inclusions and their environments. Our tentative conclusions are

- Tellurium antisites diffuse via a mercury vacancy mediated process, and therefore the diffusion coefficient is proportional to the product of the mercury vacancy and tellurium antisite concentrations.
- The migration energy of the tellurium antisite will be comparable to that of the mercury vacancy, while the overall diffusion coefficient will be much smaller.
- In HgCdTe, tellurium diffuses via tellurium antisites only; tellurium interstitial and tellurium vacancy diffusion is negligible because of the

negligible populations of these species. This conclusion is strongly supported by our work on the native defects in HgCdTe.

- A complex consisting of two tellurium antisites (each a single donor) and one mercury vacancy (a double acceptor) may be the nucleation site of a tellurium inclusion. This complex may be well bound because of its charge neutrality.
- There may be an enhanced diffusion of tellurium towards a tellurium inclusion due to a coordination of Coulomb and strain terms.
- If the tellurium antisite diffusion is very slow, as we expect, the tellurium antisites may not equilibrate during the low-temperature mercury-saturated anneals, and may in fact be the residual donor that becomes apparent when the mercury vacancy concentration is reduced below the level of 10^{15} cm^{-3} .
- We expect that the tellurium antisites are stripped out of the material in the vicinity of a tellurium inclusion by the inclusion formation process. Thus, during a low-temperature anneal, the material adjacent to the inclusion will remain mercury vacancy doped p-type after the low-temperature anneal, while the bulk will turn n-type because of the relatively high concentrations of tellurium antisites there.
- If these p-type regions about inclusions intersect one another to create p-type percolating paths, this may account for the anomalously low mobility in LPE material.

While some of the above conclusions are tentative, the picture they present is consistent with our theoretical results and the diffusion experiments. Much more work needs to be done to complete the picture. In the short term, examining the binding energy of the tellurium antisite - mercury vacancy complex will give us some further insight into the diffusion of the tellurium antisite.

2. DISLOCATIONS IN MCT

We completed a paper on our work on dislocations in HgCdTe and the way in which they impact device performance. A copy of the paper, which will be presented at the 1993 Materials IRIS meeting, is included as Appendix A.

3. TRANSPORT PROPERTIES OF HgCdTe

We have calculated the absorption coefficient, Fermi energy, Hall coefficient, and electron mobility with Fermi-Dirac statistics (FD) and accurate pseudo potential band structures fine tuned with tight-binding (TB) corrections. We have studied the

effect of the Maxwell-Boltzmann (MB) and parabolic band approximation on electron transport coefficients and on ways in which physical parameters are extracted from experiments. The values interpreted from experiments depend crucially on various approximations such as effective mass, Maxwell-Boltzmann statistics, and the collision time. Our main conclusions to date are

- Approximating the Hall factor by unity over a wide range of carrier concentrations and temperatures is accurate for most applications. An error of about 30% is expected at high temperatures and low carrier concentration (10^{14} cm^{-3}), and about 20% is expected at low T and high carrier concentration (10^{18} cm^{-3}).
- The variation of band gap with temperature is nonlinear and is faster at low temperature. The value at 22% mercury concentration is about 10 meV smaller than those usually quoted.
- The mobility calculated from a full solution to the Boltzmann transport equation with FD statistics can explain the hump near 40 K and is in good agreement with experiments. Once the other scattering mechanisms such as acoustic phonon and alloy disorder are included, the agreement is expected to be much better.

This work will be reported at the 1993 Materials IRIS meeting. A copy of the paper to be presented at that meeting is included as Appendix B.

4. WIDE-GAP II-VI COMPOUNDS (ZnSe AS PROTOTYPE)

Our computational resources have been consumed by our work on the gradient correction this quarter. As discussed above, this work on the gradient correction was necessary to provide the foundation for further work on defect formation energies. We have just resumed our work on the calculation of the defect formation energies in ZnSe. In the last quarterly, we reported on our preliminary calculation of the defect formation free energies. We have resumed these calculations to attempt to resolve discrepancies with other published work and to continue the calculation of the energy of the localized states associated with the defects.

5. NONLINEAR OPTICAL MATERIALS (LiNbO₃ AS THE PROTOTYPE)

In the previous quarter, we obtained the first-principles-based band structure for LiNbO₃. With this result in hand, we have begun our investigation of the defect structure of this compound. The difficulty of growing stoichiometric LiNbO₃ is well known. Most growth methods yield congruent lithium niobate with Li:Nb = 48.45:51.55. Although properties such as lattice parameters, density, dielectric

constant, and refractive indices depend only slightly on the Li to Nb ratio, other important properties such as optical absorption, curie point, birefringence, and nuclear magnetic resonance (NMR) line width are altered strongly by that ratio.

The deviation from stoichiometry will certainly introduce defects. Understanding the defect structure of this compound is of great device interest and the focus of the present study. There are several, often contradicting, models of the defect structure that have been proposed exclusively from experimental information. The models include Nb^{5+} residing on Li^+ sites with four lithium vacancies (for charge neutrality), arrangement of cations along the polar axis out of normal sequence with some niobium atoms on lithium sites, excess Nb with Nb_{Li} , Li^+ and O^{-2} vacancies with no stacking fault, and oxygen vacancies with one or two electrons in partially reduced lithium niobate. All these models explain a specific experiment, but an overall defect picture is not obtained. Due to sensitive dependence of various defects on growth conditions, various characterization techniques and possibly small activation energy difference, a complete defect structure is still not available. Once such a knowledge is gained, this material can be engineered more efficiently for various applications.

We have scrutinized the models proposed in the literature to identify the defects in LiNbO_3 for our initial study. We have identified the lithium vacancy (V_{Li}), the niobium antisite (Nb_{Li}), and the oxygen vacancy (V_{O}) as the first candidates for study, and have started with the lithium vacancy. The problem is approached in a supercell approach within the full-potential linearized muffin-tin orbital (LMTO) method, discussed extensively in the previous quarterlies and our proposal. We have started with the 30-atom unit cell containing one lithium vacancy. Although this corresponds to 6% vacancy concentration we have found in our work on other semiconductors that the energies from these calculations are nearly converged to the low concentration limit for the cell size quoted. When our initial survey of the primary defects is complete and the most important defects identified in our study, we will refine our calculation for the most important defects. The structure about the lithium vacancy is relaxed to minimize the defect total energy; we find that the three oxygen atoms in the plane of removed lithium move close to each other. We have encountered some numerical problems in calculating this relaxation energy, but have developed some strategies to circumvent the problems.

6. WORK PLANNED

Four papers will be presented in the next quarter, two at the 1993 Meeting of the IRIS Specialty Group on Infrared Materials, in Bedford, MA, and two at the 1993 U.S. Workshop on the Physics and Chemistry of Mercury Cadmium Telluride and other IR materials in Seattle, WA. We also plan to submit versions of these papers to the *Journal of Applied Physics*. Approval for publication and presentation of these papers has been obtained. We will be finishing our work on the gradient corrections and writing a paper on the results; this paper will be essential to the support of our work on the defects in HgCdTe , ZnSe , and LiNbO_3 . We expect to complete our paper

on defects in HgCdTe for submission to *Physical Review B* in the next quarter as well. We will begin our study of defects in CdTe this next quarter and continue our work on defects in ZnSe (in particular the localized states) and LiNbO₃.

REFERENCES

1. D. Lengreth and D. Mehl, *Phys. Rev. B* **28**, 1809 (1983).
2. A. Garcia, C. Elsässer, J. Zhu, S.G. Louie, and M.L. Cohen, *Phys. Rev. B* **46**, 9829 (1992).

Appendix A

DISLOCATIONS AND JUNCTION PERFORMANCE IN MCT

DISLOCATIONS AND JUNCTION PERFORMANCE IN MCT*

August 1993

M.W. Muller[†], A.T. Paxton[‡], A. Sher, M. Berding, M. van Schilfgaarde
SRI International, Menlo Park, CA 94025

ABSTRACT

Dislocations crossing a junction in HgCdTe have little effect on detector responsivity, but are known to reduce the zero bias impedance R_0A and increase the leakage current, especially at low temperatures where R_0A is dominated by tunneling and GR processes^{1,2}. We have calculated the core charge and piezoelectric-induced fields associated with 60° dislocations since they are superimposed on the built-in and applied junction fields that control the currents. The screening of the dislocation fields in the neutral region is nearly complete and is consistent with the dislocations' small effect on responsivity. Their impact in the space charge region is found to be significant and consistent with the nonlinear dependence of performance on dislocation density, as characterized by R_0A .

1. INTRODUCTION

The p-on-n $\text{Hg}_{1-x}\text{Cd}_x\text{Te}$ (MCT) double-layer heterojunction (DLHJ) focal plane arrays (FPAs) shown in Figure 1 are currently leading the art in long-wave infrared (LWIR) applications. The most effective structures to date are those grown by liquid-phase epitaxy (LPE) on lattice-matched CdZnTe substrates. Typical values of active (n layer) and cap (p layer) compositions are $x = 0.224$ and $x \geq 0.28$, respectively. The n layers are typically indium-doped

* This work was supported by ARPA Contract MDA972-92-C-0053.

† Permanent address: Washington University, St. Louis, MO 63130

‡ Present Address: Department of Materials, University of Oxford, OXI 3PH, UK

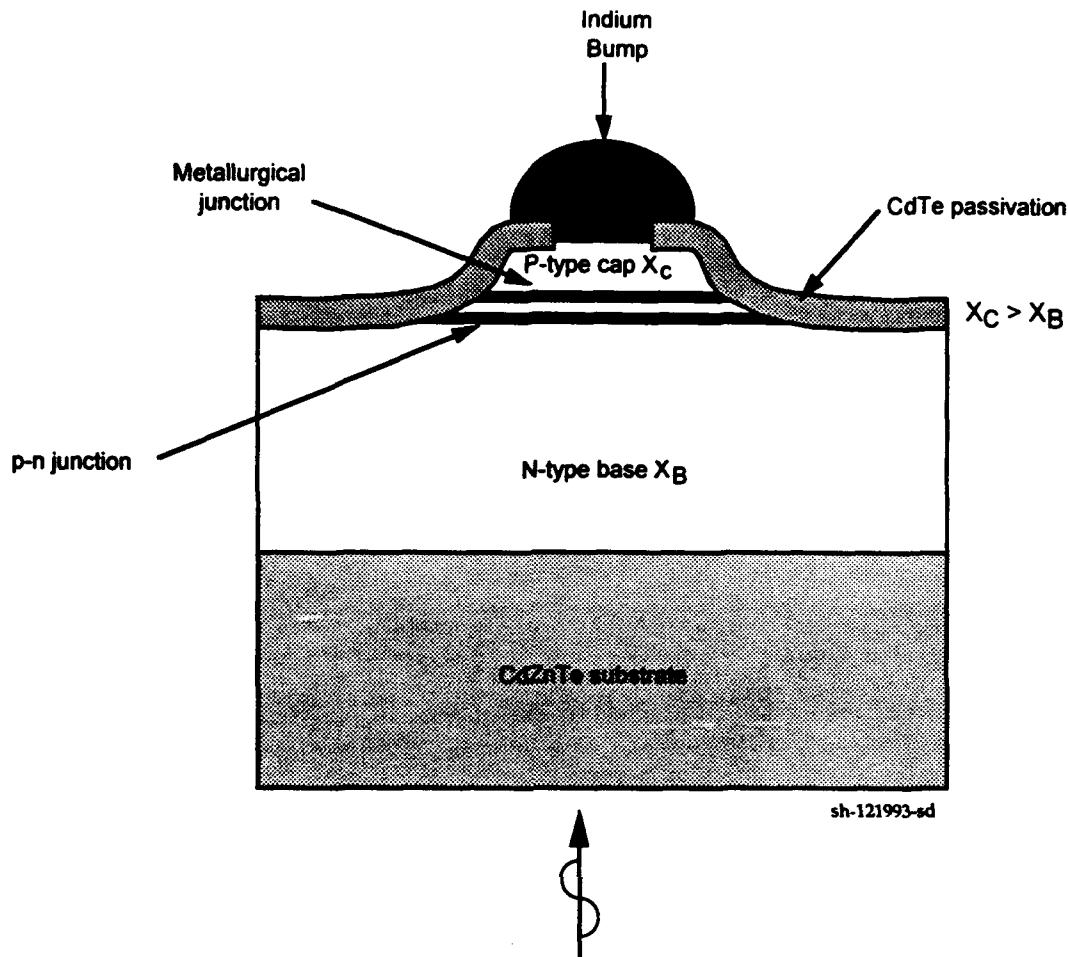


Figure 1. Cross-sectional view of DLHJ mesa diode

Source: R.E. DeWames et al., *An Assessment of HgCdTe and GaAs/GaAlAs Technologies for LWIR Infrared Imagers*, SPIE, Vol. 1735, p. 6, 1992.

in the growth process, with carrier concentrations as low as permitted by series resistance and capacitance concerns, but usually realized at $> 2 \times 10^{15} \text{ cm}^{-3}$. The cap p^+ layers are typically arsenic-doped with $p \approx 2 \times 10^{17} \text{ cm}^{-3}$. The metallurgical p-n junction is positioned on the narrow-gap side of the heterojunction, and the grading width is chosen to minimize the barrier in the valence band that occurs in such structures³, as the barrier reduces the collection efficiency of photon-induced minority carriers (holes) in the n layer from the back-lit array.

There is ample experimental evidence that dislocations degrade the performance of DLHJ detectors and may be the defects currently limiting the capabilities of the devices. The measurements that relate various material parameters pertinent to detector performance to dislocation density have been reported by several groups.^{1,2} The important, interrelated

parameters are minority carrier lifetime, zero-bias junction impedance (R_0A product), and $1/f$ noise.

Dislocations are thought to influence the electronic properties of semiconductors primarily through their electric fields. In this paper we report the results of analyses of the space charge and piezoelectric fields associated with dislocations in an attempt to understand the mechanism through which they affect the responsivity and dark currents at low temperature.

2. SUMMARY OF EXPERIMENTAL RESULTS

In the work to be discussed, dislocation densities are measured by etch pit densities (EPDs). The etch pits on the film surface are associated with threading dislocations that are assumed to penetrate the films. The relation of these dislocations to misfit dislocations and loops formed at growth interfaces is not fully understood in all cases.

Shin *et al.*² have studied the relationship between dislocation density and minority carrier lifetime in epitaxial MCT films grown by LPE, metalorganic chemical vapor deposition (MOCVD), and molecular beam epitaxy (MBE). At small dislocation densities (as measured by etch pit density) the minority carrier lifetime is not affected by the presence of dislocations, and the temperature and carrier concentration dependence of the lifetime suggests Auger recombination at high temperature (above 150 K) and Shockley-Read recombination for $T < 150$ K. However, even in samples with very low EPDs (down to pixels with no etch pits), the lifetime and the R_0A product exhibit great variability, sometimes exceeding an order of magnitude. In these high-quality samples, the transition from Auger to trap-assisted recombination can occur at temperatures as low as 60 K.⁴ We take this observation as evidence that recombination centers not associated with threading dislocations may be the defects imposing the ultimate device performance limits. In the low temperature range of interest for IR detectors, for EPD densities above the mid 10^{-5} range, minority carrier lifetime decreases with dislocation density at an $EPD^{-2/3}$ to $EPD^{-3/4}$ rate. Shin *et al.*² note that the observed behavior is consistent with dislocations acting as Shockley-Read recombination centers with a trap level 60 meV above the valence band edge and a trap density proportional to $EPD^{-3/4}$. Although not explicitly stated in this paper, the results reported suggest that dislocations active as recombination centers are likely to carry a core charge. Similar results have been reported by Baranskii *et al.*⁵ who find that mobile dislocations introduced in bulk MCT by indentation give rise to a trapping level at $E_v + 50$ meV.

Johnson *et al.*¹ have measured the dependence of R_0A in arrays of photovoltaic diodes on dislocation density by deliberately using plastic deformation to introduce dislocations in localized regions and carrying out the measurement on both high and low EPD diodes of the same array. They find that the resistance is relatively insensitive to EPD at the lowest dislocation densities, decreases linearly at higher densities, and decreases quadratically at the highest densities. The nonlinear behavior sets in at small dislocation densities (mid 10^5 cm^{-2} or less) at low temperature (40 K) and at higher densities ($>10^6 \text{ cm}^{-2}$) at 78 and 120 K. Measurements of the temperature dependence of the leakage current of diodes with different dislocation densities show that the high temperature (diffusion regime) R_0A is not affected by the presence of dislocations, but that as the temperature is reduced below 150 K the R_0A values diverge, differing by several orders of magnitude at 40 K and below. The authors interpret the low temperature leakage current as generation-recombination current. They adopt a model (Zolper and Barnett⁶) for estimating the reduction of the minority carrier diffusion length by recombination at dislocations, and then account for the inverse quadratic increase of the short circuit current at high dislocation densities by the *ad hoc* assumption that closely spaced dislocation pairs contribute a conductance that exceeds the sum of the conductances of two individual dislocations. We shall point out below that such nonlinear behavior may be a feature of tunneling currents associated with dislocations. The same work also reports on measurements of $1/f$ noise. The noise current was found to be proportional to the leakage current, leading to the conclusion that the dislocations act only as indirect noise sources by increasing the leakage current.

3. CALCULATION OF DISLOCATION PROPERTIES

We wish to distinguish between dislocations that intersect the junction and those that do not. We shall refer to intersecting dislocations as *threading dislocations*. Threading dislocations eventually intersect the surface of the device, and therefore are observable by etch pits. Such dislocations have a number of sources. They can originate in the substrate and propagate through the active material during growth; they can be introduced by plastic deformation of the material; or they can originate from lattice or thermal mismatch in the structure.

3.1 DISLOCATION CORES

Classical elasticity theory works well for the description of long-range strain fields of dislocations in real solids, but fails when it comes to a description of the dislocation core. The description of dislocation cores necessarily depends on the microscopic properties of the

materials. If we view the 60° dislocation as the removal of three $\{112\}$ -type half-planes of atoms, followed by the displacement and rejoining of the crystal across the missing plane, the line that describes the termination of the missing plane is the dislocation line. The dislocation core is the cylindrical volume centered at the dislocation line; in that core, bonds are broken, displacements of atoms are large, and displacements cannot be described by linear elastic theory. Because broken bonds are present in the cores, localized states can be introduced in the band gap. Although reconstruction may take place to move these states out of the gap, it is not clear whether this occurs in MCT.

For the undissociated 60° dislocation in MCT, the local states of dislocation cores will depend on the plane on which the extra half-planes of atoms terminate (i.e., whether they are cation or anion terminated), and whether the dislocation belongs to the shuffle or glide set. Dislocations of the glide set in the group IV and III-V semiconductors are frequently found to be dissociated into two Shockley partials separated by a stacking fault. One study on GaAs found that as many as 80% of the 60° dislocations in plastically deformed GaAs were dissociated⁷. It is not clear whether the majority of the 60° dislocations in MCT are dissociated, but is likely that they are. Since the primary effects of the space charge and piezoelectric fields considered here occur at the longer range, where classical elasticity is valid, the effects considered in this work differ little between an undissociated dislocation and a pair of partials.

3.2 CHARGED DISLOCATIONS

The Coulomb fields associated with electrically charged dislocation cores can act as scattering and recombination centers and may attract or repel charged point defects. The presence and amount of charge on a dislocation core depends on the distribution of localized levels in the bandgap in the core and on the Fermi level in the semiconductor. Once the core structure of the dislocation has been determined, we can take a phenomenological view and consider only the electric field and potential generated by a given core charge. The effective radius of the field is taken to be that distance from the dislocation core within which the field is large enough to move a minority carrier to the core in a carrier lifetime as measured in the dislocation-free material. In this way we define a volume within which the lifetime and mobility are affected by the presence of a charged dislocation. Only if the affected volume surrounding all the dislocations is a significant fraction of the total volume can we expect their presence to affect lifetime and mobility and hence R_0A . This then relates the depletion radius R or screening radius ℓ to a threshold of the dislocation density n_D .

We represent the dislocation core by a cylindrical charge density $-p$ in a cylinder of radius a in n -type material with donor density n . The potential distribution in the depletion approximation is given by the Poisson equation with charge density p :

$$\begin{aligned}
\rho &= (-p + n)e & r < a \\
&= ne & a < r < R \\
&= 0 & R < r
\end{aligned}$$

where R is the depletion radius, related to a by the charge neutrality requirement $pa^2 = nR^2$. By integrating the Poisson equation we find for the potential

$$\phi(r) = \phi(a) + \frac{en}{2\epsilon} \left[R^2 \ln \frac{r}{a} - \frac{1}{2}(r^2 - a^2) \right]$$

and taking the potential in the bulk ($r \geq R$) as reference, we can evaluate the potential at the core radius

$$\phi(a) = \frac{en}{2\epsilon} \left[\frac{1}{2}(R^2 - a^2) - R^2 \ln \frac{R}{a} \right].$$

Using a dislocation core radius of 5×10^{-8} cm and assuming the bands bend by the bandgap—that is, by a potential (relative to the bulk) at the core radius of 0.1 V for 8- to 12- μ m material, we have calculated R as a function of carrier density, as shown in Figure 2. It turns out that the radius is close enough to the Debye length to make the depletion approximation questionable.

The exact space charge equation is

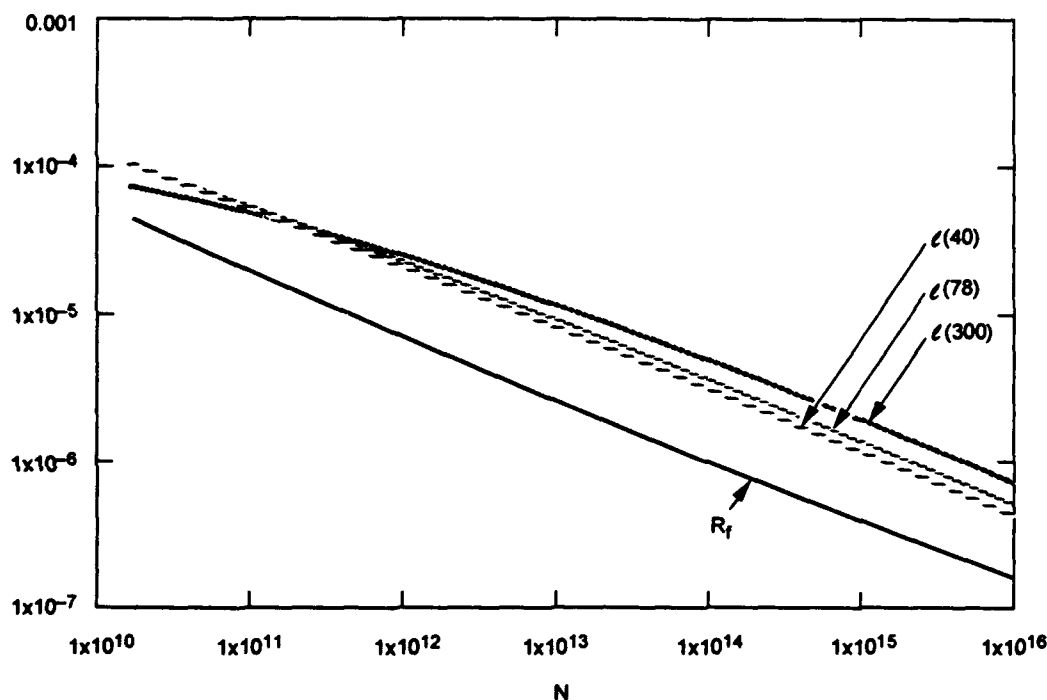
$$\frac{1}{r} \frac{d}{dr} r \frac{d\phi}{dr} = \frac{2}{L^2} [\sinh(\phi - \phi_F) - \sinh \phi_F]$$

where

$$\phi = \frac{e\phi}{kT}, \quad L^2 = \frac{\epsilon kT}{e^2 n_i}, \quad \phi_F = \frac{E_F - E_i}{kT} = \sinh^{-1} \frac{N_D - N_A}{n_i}.$$

For ϕ small this is

$$\frac{1}{r} \frac{d}{dr} r \frac{d\phi}{dr} \approx \left(\frac{2}{L^2} \cosh \phi_F \right) \phi = \frac{2}{L_D^2} \phi$$



mu-072893-jd

Figure 2. Depletion radius R and screening radius ℓ (meters) at 40, 78, and 300 K as functions of carrier density in cm^{-3}

with the extrinsic Debye length

$$L_D^2 = \frac{L^2}{\cosh \phi_F} \equiv \frac{\epsilon k T}{e^2 N_D} = \frac{2.77 \times 10^5}{N_D}, \quad N_D \text{ in } \text{cm}^{-3}.$$

Then with $x = \frac{r}{L_D}$ we have $\frac{1}{x} \frac{d}{dx} x \frac{d\phi}{dx} = \phi$, the zero-order modified Bessel equation. The solution of interest is the decreasing Hankel function $K_0(x)$.

The depletion approximation should be valid for $r < R - L_D$. This does not leave much room since R and L_D are comparable. One way to proceed is to let $\phi = CK_0(x)$ and to evaluate C from $\phi(a)$ at $x = a/L_D$. Since the value of x here is that at the core radius, x is small and we can use

$$K_0(x) \equiv \ln(\gamma x) = 0.116 - \ln x,$$

so

$$K_0\left(\frac{a}{L_D}\right) = 0.116 + \ln\left(\frac{a}{L_D}\right) = \frac{\phi(a)}{C}$$

to determine C. The effective scattering radius of the dislocation can be obtained from the radius at which the field is reduced to the threshold value discussed above, here denoted E.

$$E = \frac{d\phi}{dr} = \frac{kT}{e} \frac{d\phi}{dr} = \frac{kT}{eL_D} \frac{d\phi}{dx} = \sqrt{\frac{nkT}{\epsilon}} CK_1(x)$$

where n is the carrier density. Here the argument of the Bessel function corresponds to the screening radius, so x is large, and we can use

$$K_1(x) \cong \sqrt{\frac{\pi}{2x}} e^{-x}$$

Finally we obtain the screening radius $\ell = L_D x$ from the solution of

$$\sqrt{\frac{nkT}{\epsilon}} C \sqrt{\frac{\pi}{2x}} e^{-x} = E.$$

The threshold field E is now determined, as discussed above, from the mobility μ and lifetime τ in dislocation-free material

$$E = \ell/\mu\tau = L_D x/\mu\tau.$$

This is substituted in the immediately preceding expression, and the resulting expression solved for the normalized screening radius x. The screening radius ℓ as a function of n is plotted for T = 40 K, 78 K, and 300 K in Figure 2. In the calculation we have used the exact values of the Bessel functions rather than the approximations show above, and the following values of mobility and lifetime:

T, K	μ , cm ² /Vs	τ , s
40	1.9×10^5	1×10^{-6}
78	9×10^4	3×10^{-7}
300	1×10^4	1×10^{-7}

As expected, ℓ turns out to be larger than the depletion radius, confirming the need for the more accurate screening theory. The figure shows the results of both calculations: the radius R of the field region surrounding the positively charged core as a function of carrier density calculated on the basis of the depletion approximation, and the screening radius ℓ of the region inside which the electric field due to the charged core exceeds the critical value. The threshold is consistent with the experimental observations^{1,4} that the R_0A values and minority-carrier lifetimes decrease rapidly with the dislocation density n_D when it exceeds 10^6 cm⁻². The

calculation of the screening radius ℓ is more reliable than the depletion approximation, since it takes into account the thermal excitations of the carriers. With the parameters we use, the calculation of the screening radius over five orders of magnitude of the carrier density, and over the temperature range from 40 to 300 K, results in values of ℓ that range from about $5 L_D$ at $n = 10^{10} \text{ cm}^{-3}$ to $10 L_D$ at $n = 10^{15} \text{ cm}^{-3}$, resulting in an overall rate of decrease of ℓ with carrier density at a rate slightly slower than $L_D^{-1/2}$.

The carrier density in the neutral region of the extrinsic device material generally equals or exceeds 10^{14} cm^{-3} . The screening length at this carrier density, even at room temperature, is less than $5 \mu\text{m}$, and it is only about $3 \mu\text{m}$ at 40 K. Since the mobile carrier density in the neutral regions generally exceeds 10^{14} cm^{-3} , we can conclude that in the presence of mobile carriers, especially at cryogenic temperatures, the core charge fields have a limited range. This is also consistent with the observations of Johnson *et al.*¹ that the responsivity of p on n heterojunction devices (dependent on diffusion in the neutral region) is little affected even by high dislocation densities.

The situation is less clear in the vicinity of the metallurgical junction of the p-n diode detector. In this region, the carrier density is reduced to the intrinsic value n_i under zero bias, and below that with reverse bias. We estimate a value of n_i about $5 \times 10^{11} \text{ cm}^{-3}$ for $\text{Hg}_{0.8}\text{Cd}_{0.2}\text{Te}$ at 40 K, with a decrease of about a factor of 2 for every 5 mV of reverse bias caused by the separation of the quasi-Fermi levels. This reduction of the carrier density is confined to a small region, and an assessment of its quantitative effect will require detailed computation. Nonetheless, it is worth observing that we estimate a screening radius of $27 \mu\text{m}$ for this carrier density. This is consistent with the experimental finding⁴ that R_0A at this temperature is already decreasing with dislocation densities in the 10^5 cm^{-2} range, corresponding to this order of separation between dislocation lines. The literature values of $n_i = 1.2 \times 10^{14} \text{ cm}^{-3}$ at 77 K and $n_i = 4.0 \times 10^{16} \text{ cm}^{-3}$ at 300 K⁷ correspond to progressively shorter screening lengths, which is also consistent with the experimental observation that the decrease in R_0A with dislocation density has a higher threshold at the higher temperature.

The transition from the neutral to the depleted region is not abrupt, so that the screening is a function of both the distance from the dislocation core and the distance from the junction plane. For a dislocation perpendicular to the junction plane, the geometry has cylindrical symmetry, making it effectively two-dimensional. The geometry is more complicated for a dislocation inclined relative to the junction plane.

Because its form is geometrically simpler and more readily visualizable in this context, we have discussed screening entirely in connection with the effect of core charges. It should be kept in mind that similar, although quantitatively different, considerations apply to the screening of the piezoelectrically induced potentials, to be discussed next.

3.3 DISLOCATION STRAIN FIELDS AND PIEZOELECTRIC POTENTIALS

The MCT crystal structure lacks inversion symmetry and is therefore piezoelectric. In a piezoelectric crystal the strain field around a dislocation may generate an electric field.

Conversely, an electric field applied to a piezoelectric crystal can produce a stress that may deform the crystal. This self-consistent field problem has been treated rigorously for a straight dislocation in a homogeneous insulating crystal by Saada⁸. The general analysis was extended by Faivre and Saada⁹ to include the effects of screening by free carriers. Several qualitatively significant conclusions can be drawn from this work:

1. The strains are only slightly affected by the electric field; that is, the inverse piezoelectric effect is small, and the electric field can be calculated directly without imposing the requirement of self-consistency.
2. The electric field in the vicinity of the dislocation core can be quite large, and the dislocation can interact strongly with charges (point defects or mobile carriers) in its vicinity.
3. In a semiconductor, the dislocation preferentially traps carriers of a particular sign.
4. The estimated screening distance is of the order of several Debye lengths.

Booyens and Vermaak¹⁰ have applied Saada's analysis to $\langle 110 \rangle / \langle 111 \rangle$ dislocations in zinc blende III-V semiconductors and Booyens and Basson¹¹ to CdTe and MCT. They do not explicitly include the effects of screening as analyzed by Faivre and Saada⁸ in these calculations. As a result, they find that an uncharged dislocation, in the absence of screening, generates a net radial field. They then suggest that the dislocation core is likely to acquire a charge that compensates for the radial field and so minimizes the total energy of the dislocation.

We have extended the analysis to the commonly observed 60° dislocations in intrinsic MCT. The dislocation lies along $[T01]$ and has a Burgers vector b at 60° to the dislocation line ξ . x_1 is chosen parallel to the edge component of the Burgers vector b ; x_2 is chosen as the normal to the slip plane; and x_3 is chosen parallel to ξ . The transformation matrix from principal axis coordinates is

$$T_{ij} = \frac{1}{\sqrt{6}} \begin{pmatrix} 1 & -2 & 1 \\ \sqrt{2} & \sqrt{2} & \sqrt{2} \\ -\sqrt{3} & 0 & \sqrt{3} \end{pmatrix},$$

and thus the transformation of the piezoelectric tensor is

$$d'_{ijk} = T_{ip} T_{jq} T_{kr} d_{pqr}.$$

In cubic symmetry and principal axis coordinates, all the nonzero components of the piezoelectric tensor are equal: $d_{123}=d_{132}=d_{231}=d_{213}=d_{312}=d_{321}=d$. The nonzero components of the transformed tensor are

$$\begin{aligned} d'_{133} &= d'_{313} = d'_{331} = -d'_{111} = \frac{2}{\sqrt{6}}d \\ d'_{112} &= d'_{121} = d'_{211} = d'_{233} = d'_{323} = d'_{332} = \frac{1}{\sqrt{3}}d \\ d'_{222} &= \frac{2}{\sqrt{3}}d; \end{aligned} \quad (1)$$

or, using two-index (Voigt) notation,

$$(d') = \begin{pmatrix} -\frac{2}{\sqrt{6}}d & 0 & \frac{2}{\sqrt{6}}d & 0 & 0 & -\frac{1}{\sqrt{3}}d \\ -\frac{1}{\sqrt{3}}d & \frac{2}{\sqrt{3}}d & -\frac{1}{\sqrt{3}}d & 0 & 0 & 0 \\ 0 & 0 & 0 & -\frac{1}{\sqrt{3}}d & \frac{2}{\sqrt{6}}d & 0 \end{pmatrix}.$$

The piezoelectrically induced bound charge density is¹²

$$\rho(r) = \frac{1}{\epsilon} d'_{ijk} e_{jk,i} \text{ with } e_{jk,i} \equiv \frac{\partial}{\partial x_i} e_{jk} \quad (2)$$

where ϵ is the isotropic dielectric constant, e_{jk} is the jk component of the strain tensor, and summation over repeated indexes is implied.

For a screw dislocation in linear anisotropic theory, the displacements are

$$u_3 = -\frac{b_s}{2\pi} \tan^{-1} A \left(\frac{x_2}{x_1} \right),$$

$$u_1 = u_2 = 0,$$

where b_s is the magnitude of the screw component of the Burgers vector and

$$A = \frac{\sqrt{c'_{44}c'_{55}}}{c'_{44}}; \quad c'_{44} = c_{44} - \frac{1}{3}H; \quad c'_{55} = c_{44} - \frac{1}{6}H; \quad H = 2c_{44} + c_{12} - c_{11}.$$

Here c_{ij} and c'_{ij} are the components of the elastic tensor in the principal axis and transformed coordinate systems respectively. The nonzero components of the strain tensor are [using $e_{ij} = \frac{1}{2}(u_{i,j} + u_{j,i})$]

$$e_{13} = e_{31} \text{ and } e_{23} = e_{32}.$$

Using Eqs. 1 and 2 shows immediately that for this case $r = 0$. Even in anisotropic linear elasticity (assuming the dielectric constant isotropic) the screw component of the 60° dislocation induces no piezoelectric effect. Therefore, pure screw $\langle 110 \rangle$ dislocations will also show no piezoelectric activity even if they are dissociated. We now proceed to consider the edge component, which we will simply denote b . In order to arrive at a transparent expression, we will make the isotropic elastic approximation. This will not affect the order of magnitude calculations that follow.

For an edge dislocation, with ν Poisson's ratio

$$\begin{aligned} u_1 &= \frac{b}{2\pi} \left[\tan^{-1} \left(\frac{x_2}{x_1} \right) + \frac{x_1 x_2}{2(1-\nu)(x_1^2 + x_2^2)} \right]; \\ u_2 &= -\frac{b}{2\pi} \left[\frac{1-2\nu}{4(1-\nu)} \ln(x_1^2 + x_2^2) + \frac{x_1^2 - x_2^2}{4(1-\nu)(x_1^2 + x_2^2)} \right]; \\ u_3 &= 0. \end{aligned}$$

The nonzero strain components are

$$\begin{aligned} e_{11} &= \frac{b}{2\pi} \frac{(1-2\nu)x_2^3 + (3-2\nu)x_1^2 x_2}{2(\nu-1)(x_1^2 + x_2^2)^2} \\ e_{22} &= \frac{b}{2\pi} \frac{(1-2\nu)x_2^3 - (1+2\nu)x_1^2 x_2}{2(\nu-1)(x_1^2 + x_2^2)^2} \\ e_{12} &= \frac{b}{2\pi} \frac{x_1 x_2^2 - x_1^3}{2(\nu-1)(x_1^2 + x_2^2)^2} . \end{aligned}$$

From Eqs. 2 and 1,

$$\rho(r) = \frac{1}{\epsilon} (d'_{111} e_{11,1} + 2d'_{112} e_{12,1} + d'_{211} e_{11,2} + d'_{222} e_{22,2})$$

so we need the derivatives

$$e_{11,1} = \frac{b}{2\pi} \frac{(2v+1)x_1x_2^3 + (2v-3)x_1^3x_2}{(v-1)(x_1^2+x_2^2)^3}$$

$$e_{11,2} = \frac{b}{2\pi} \frac{(2v-1)x_2^4 - 6x_1^2x_2^2 + (3-2v)x_1^4}{2(v-1)(x_1^2+x_2^2)^3}$$

$$e_{22,2} = \frac{b}{2\pi} \frac{(2v-1)x_2^4 + 6x_1^2x_2^2 - (2v+1)x_1^4}{2(v-1)(x_1^2+x_2^2)^3}$$

$$e_{12,1} = \frac{b}{2\pi} \frac{x_2^4 - 6x_1^2x_2^2 + x_1^4}{2(v-1)(x_1^2+x_2^2)^3}$$

giving

$$\begin{aligned} \rho(x_1, x_2) &= \frac{d}{\sqrt{3}\epsilon} (-\sqrt{2} e_{11,1} - 2e_{12,1} - e_{11,2} + 2e_{22,2}) \\ &= \frac{bd}{2\pi\sqrt{3}\epsilon} \frac{(2v-3)x_2^4 - 2\sqrt{2}(2v+1)x_1x_2^3 + 30x_1^2x_2^2 + 2\sqrt{2}(3-2v)x_1^3x_2 - (2v+7)x_1^4}{2(v-1)(x_1^2+x_2^2)^3} \end{aligned}$$

When this expression is converted to polar coordinates in the x_1x_2 plane, it becomes somewhat simpler:

$$\rho = \frac{bd}{2\pi\sqrt{3}\epsilon} (\rho_1 + \rho_2 + \rho_3 + \rho_4 + \rho_5)$$

with

$$\rho_1 = \frac{(2v-3)}{2(v-1)} \frac{y^4}{r^6} = \frac{(2v-3)}{2(v-1)} \frac{\cos 4\theta - 4\cos 2\theta + 3}{8r^2}$$

$$\rho_2 = \frac{-2\sqrt{2}(2v-1)}{2(v-1)} \frac{xy^3}{r^6} = \frac{-2\sqrt{2}(2v-1)}{2(v-1)} \frac{2\sin 2\theta - \sin 4\theta}{8r^2}$$

$$\rho_3 = \frac{30}{2(v-1)} \frac{x^2y^2}{r^6} = \frac{30}{2(v-1)} \frac{1 - \cos 4\theta}{8r^2}$$

$$\rho_4 = \frac{2\sqrt{2}(3-2\nu)}{2(\nu-1)} \frac{x^3 y}{r^6} = \frac{2\sqrt{2}(3-2\nu)}{2(\nu-1)} \frac{\sin 4\theta + 2\sin 2\theta}{8r^2}$$

$$\rho_5 = \frac{-(2\nu+7)}{2(\nu-1)} \frac{x^4}{r^6} = \frac{-(2\nu+7)}{2(\nu-1)} \frac{\cos 4\theta + 4\cos 2\theta + 3}{8r^2}$$

so

$$\rho = \frac{bd}{4\pi\sqrt{3}\epsilon(1-\nu)} \frac{1}{r^2} [5\cos 4\theta - \sqrt{2}\sin 4\theta + 2(1+\nu)\cos 2\theta - \sqrt{2}(1-2\nu)\sin 2\theta]$$

$$= \frac{C}{r^2} \sum_{n=2,4} [a_n \cos(n\theta) + b_n \sin(n\theta)]$$

which defines a useful constant C, and four parameters depending only on Poisson's ratio. This simple expression reveals the charge density to have an inverse square decay and quadrupole and hexadecapole terms only. Note in particular that there is no monopole term and hence no net charge induced on the dislocation line. This rather transparent expression has not been revealed in previous work^{10,11}.

To obtain the piezoelectric potential we need to solve the Poisson equation

$$\nabla^2 \Phi = -\frac{4\pi\rho}{\epsilon}$$

with this charge distribution as the source. In two dimensions, the formal solution of the Poisson equation is

$$\begin{aligned} \Phi(r, \theta) &= \frac{1}{\pi} \int_0^\infty r' dr' \int_0^{2\pi} d\theta' \left[\ln \frac{1}{r_>} + \sum_{m=1}^\infty \frac{1}{m} \left(\frac{r_<}{r_>} \right)^m \cos m(\theta - \theta') \right] \rho(r') \\ &= \frac{C}{\pi} \sum_{m=1}^\infty \frac{1}{m} \int_0^{2\pi} d\theta' [\sin(m\theta)\sin(m\theta') + \cos(m\theta)\cos(m\theta')] \times \\ &\quad \times \sum_{n=2,4} [a_n \cos(n\theta') + b_n \sin(n\theta')] \int_0^\infty \frac{r' dr'}{r'^2} \left(\frac{r_<}{r_>} \right)^m \end{aligned}$$

where $r_>$ and $r_<$ are the greater and lesser, respectively, of r and r' .

In analogy with the solution for the elastic field, the integrand diverges at the origin and is also not normalizable. To deal with this difficulty, we adopt the same procedure that is used to

avoid the divergence of the elastic energy of a dislocation at the origin in continuum theory. We set cutoffs at an inner radius, R_1 , and an outer radius, R_2 . The cutoff at R_1 removes the core singularity and the cutoff at R_2 allows ρ to be expanded in multipoles. Later, we will identify R_1 as the core radius and we will let $R_2 \rightarrow \infty$. We now have

$$\begin{aligned}\Phi(r, \theta) &= \frac{C}{\pi} \sum_{n=2,4} \frac{\pi}{n} \left[a_n \cos(n\theta) + b_n \sin(n\theta) \right] \left(\frac{1}{r^n} \int_{R_1}^r (r')^{n-1} dr' + r^n \int_r^{R_2} (r')^{-n-1} dr' \right) \\ &= C \left\{ \frac{1}{4} [a_4 \cos(4\theta) + b_4 \sin(4\theta)] \left[\frac{1}{2} - \frac{1}{4} \left(\frac{R_1}{r} \right)^4 - \frac{1}{4} \left(\frac{r}{R_2} \right)^4 \right] \right. \\ &\quad \left. + \frac{1}{2} [a_2 \cos(2\theta) + b_2 \sin(2\theta)] \left[1 - \frac{1}{2} \left(\frac{R_1}{r} \right)^2 - \frac{1}{2} \left(\frac{r}{R_2} \right)^2 \right] \right\}\end{aligned}$$

for $r < R_2$. For $r > R_2$

$$\begin{aligned}\Phi(r, \theta) &= C \left\{ \frac{1}{4} [a_4 \cos(4\theta) + b_4 \sin(4\theta)] \frac{1}{4} \left[\left(\frac{R_2}{r} \right)^4 - \left(\frac{R_1}{r} \right)^4 \right] \right. \\ &\quad \left. + \frac{1}{2} [a_2 \cos(2\theta) + b_2 \sin(2\theta)] \frac{1}{2} \left[\left(\frac{R_2}{r} \right)^2 - \left(\frac{R_1}{r} \right)^2 \right] \right\}\end{aligned}$$

which is a multipole potential. The two solutions are matched at R_2 . We can now let $R_2 \rightarrow \infty$ and neglect the terms in R_1 , which amount to a small correction near the core, to get a potential valid for $r \gg R_1$

$$\Phi(r, \theta) = C \left\{ \frac{1}{8} [a_4 \cos(4\theta) + b_4 \sin(4\theta)] + \frac{1}{2} [a_2 \cos(2\theta) + b_2 \sin(2\theta)] \right\}$$

which is independent of r . This rather surprising behavior is a consequence of the inverse square decay of the charge density. In this connection, we can pursue the analogy with the well-known elastic solution for an edge dislocation by pointing out that while the elastic energy per unit length is given by (μ is the isotropic shear modulus)

$$\frac{\mu b^2}{4\pi(1-\nu)} \left(\ln \frac{R_2}{R_1} - 0.5 \right)$$

the piezoelectric energy per unit length is (where C was defined earlier, and taking $\nu = 0.3$)

$$\frac{9\pi^2 C^2}{1.6} \left(\ln \frac{R_2}{R_1} - 0.125 \right)$$

which is six orders of magnitude smaller—justifying our neglect of the reverse piezoelectric effect. In both cases, the first term comes from the energy in an infinite cylinder integrated to R_2 and which diverges logarithmically, and the second term is the effect of the cylindrical surface bounding this dislocation in a finite crystal (the image term).

For a good numerical calculation, we would need the piezoelectric constant of the alloy, which has not been determined. For an order-of-magnitude estimate, we can use the piezoelectric constant of CdTe, $3 \times 10^{-6} \text{ C cm}^{-2}$. The Burgers vector is $4 \times 10^{-8} \text{ cm}$, and Poisson's ratio can be taken as 0.3. Using these values we have computed the charge, potential, and field, shown in Figure 3.

It should be understood that because of the symmetry of the strain field associated with a straight dislocation, several of the possible sources of the piezoelectric potential are identically zero. In the reduced symmetry of curved dislocations (e.g., misfits), kinks, and jogs, these components of the potential do not vanish and may be significant.

3.4 AVERAGING NONLINEAR EFFECTS

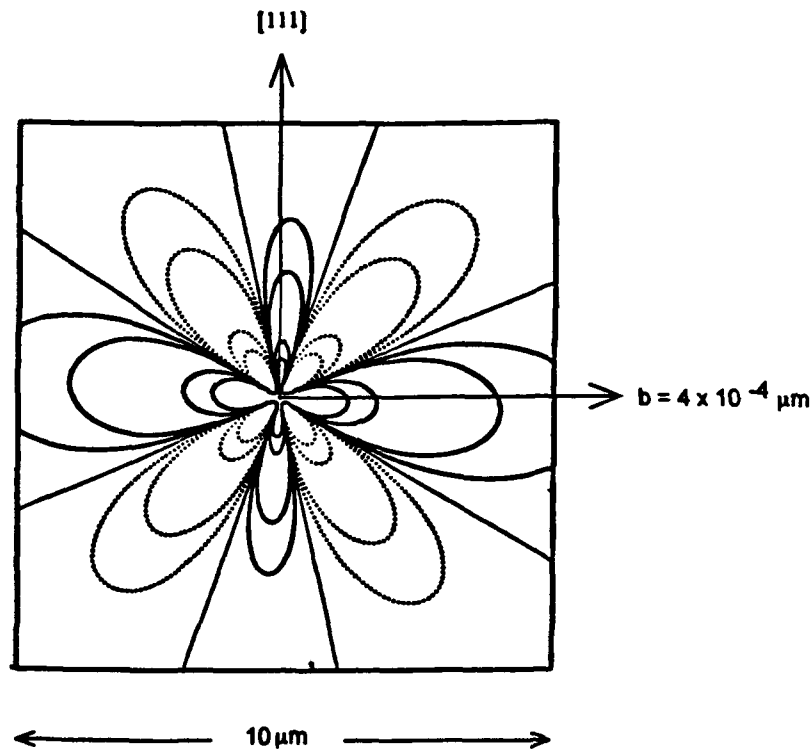
The results we have obtained afford a qualitative insight into the effect of the piezoelectric potential on the characteristics of a pn junction threaded by a dislocation. The angular variation of the potential will alternately add to and subtract from the built-in potential of the junction, so that the barrier seen by a carrier crossing the junction will depend on its trajectory. Because of the strongly nonlinear dependence of both diffusion and tunneling currents on the barrier, the effect of such a barrier variation does not average to zero and the currents can be enhanced by a large factor. To illustrate the principle, we choose as an example the average tunneling probability for carriers crossing a narrow semiconductor junction.

The band-to-band tunneling probability has the form

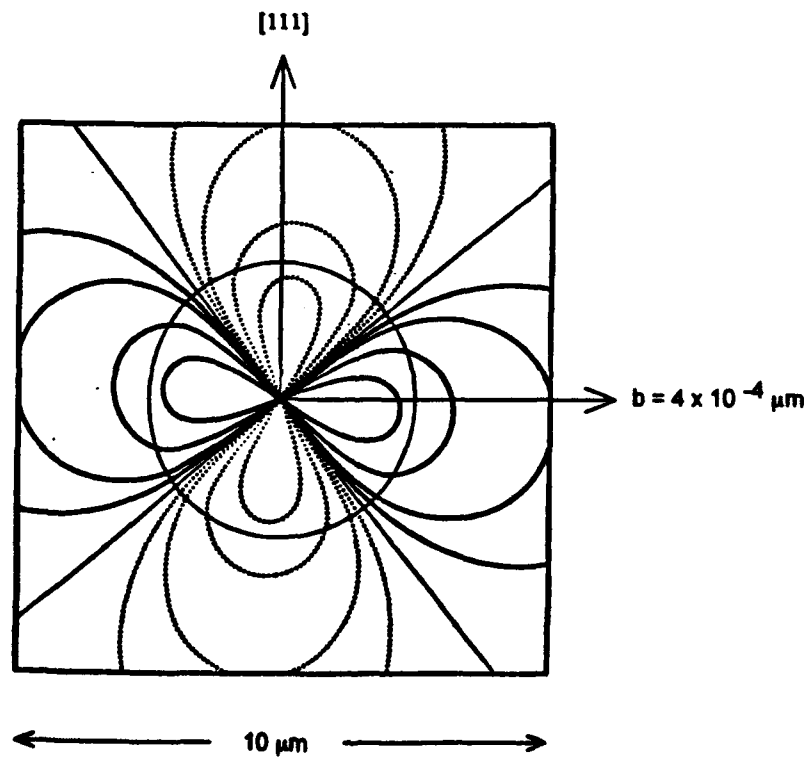
$$p = \exp(-CE_g^{3/2})$$

where E_g is the bandgap and C is a constant containing all other material parameters.

We crudely represent the effect of the dislocation potential, which makes the tunneling barrier a function of the carrier's trajectory, as an angular variation of the bandgap of the form $E_g = E_{g0}(1 + \Delta \sin \theta)$ (it will be apparent presently that the detailed form of the angular variation is irrelevant for this argument). It is likely that this representation of the piezoelectric potential introduced by a dislocation can probably be justified by a WKB calculation.

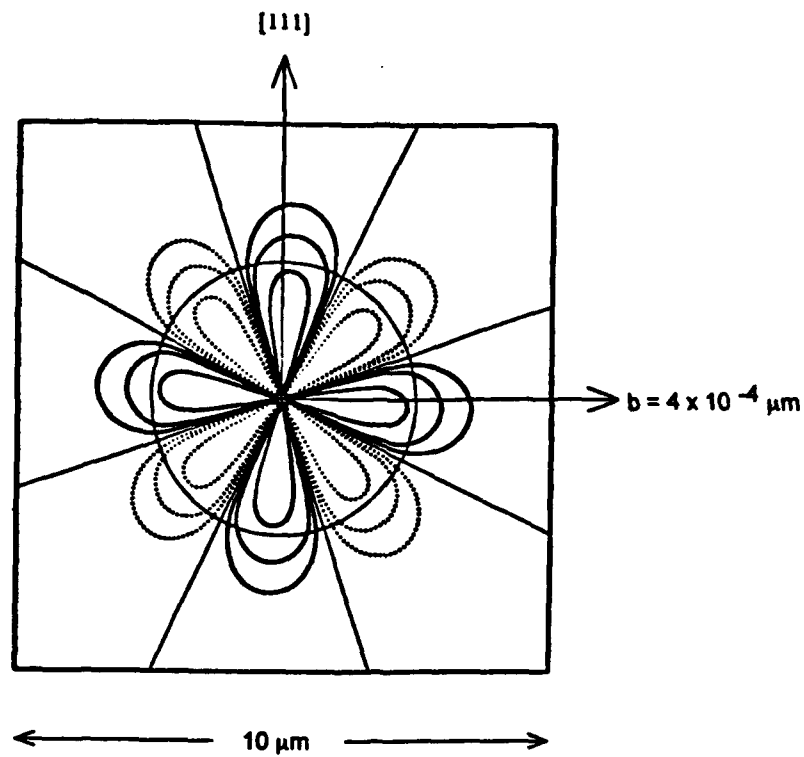


(a) Piezoelectric charge normal to the dislocation line. Solid contours are 1, 0.5, 0.1, and 0.05 10^{12} e/cm³ going out radially; dotted contours are the negative of these.

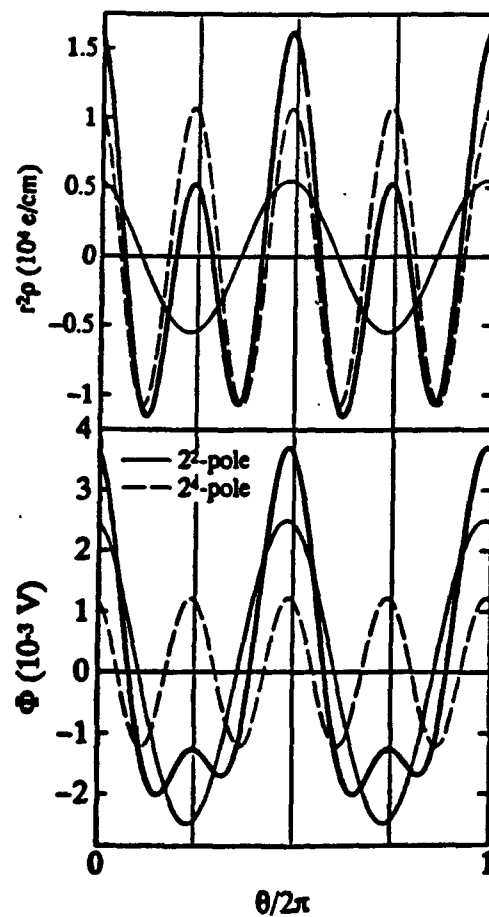


(b) Quadrupole component of the piezoelectric potential.

Figure 3. Piezoelectric properties of a 60° dislocation in $\text{Hg}_{0.8}\text{Cd}_{0.2}\text{Te}$



(c) Hexadecapole component of the piezoelectric potential



(d) Angular variation of the piezoelectric charge and potential normal to the dislocation line

Figure 3 (continued). Piezoelectric properties of a 60° dislocation in $\text{Hg}_{0.8}\text{Cd}_{0.2}\text{Te}$

If Δ is small compared with unity we have

$$E_g^{3/2} = E_{g0}^{3/2} \left(1 + \frac{3}{2} \Delta \sin \theta \right)$$

(this approximation is taken purely to simplify the mathematics and has no effect on the argument). We can now compute an average of p

$$\langle p \rangle = \frac{1}{2\pi} \int_0^{2\pi} \exp \left[-CE_{g0}^{3/2} \left(1 + \frac{3}{2} \Delta \sin \theta \right) \right] d\theta = \frac{p_0}{2\pi} \int_0^{2\pi} \exp \left[-\frac{3}{2} CE_{g0}^{3/2} \Delta \sin \theta \right] d\theta = p_0 I_0 \left(\frac{3}{2} CE_{g0}^{3/2} \Delta \right)$$

where $I_0(x)$ is the modified zero-order Bessel function and p_0 is the tunneling probability in the absence of any dislocations. From this last form it can be seen that the average tunneling probability could have been written as

$$\langle p \rangle = p_0 I_0 \left(\frac{3}{2} \Delta \ln |p_0| \right).$$

It can be seen that although the fractional bandgap "angular modulation" Δ is small, the argument of the Bessel function need not be, and the factor multiplying the unmodulated bandgap transition probability can be quite large. It is also evident that any other angular variation would lead to very similar results. The angular variation Δ can be estimated from the angular potential plots of Figure 3 to be roughly 0.05 to 0.1. The parameters determining p_0 (e.g., effective mass, doping, temperature) cover a wide range. For typical values of these parameters the multiplying Bessel function ranges from near unity to about 10, so $\langle p \rangle / p_0$ is in rough agreement with the observed¹ effect of a single dislocation on R_0A of a pixel.

As another consequence of the type of nonlinearity examined here, the effect of overlapping piezoelectric potentials of neighboring dislocations is expected to be enhanced over what might be expected from a linear superposition. This may be a possible clue to the observed inverse faster than linear falloff of R_0A with dislocation density.

4. CONCLUSIONS

We have evaluated the electric fields associated with dislocation charges and strain fields, and estimated their effects on junction performance. We conclude that the fields associated with core charges alone are not likely to account for the observed degradation of junction performance, particularly when the lower carrier concentration is on the n side of the junctions so

the principal minority carriers are holes. The longer range piezoelectric potentials, which we have calculated explicitly for the common 60° dislocation, are likely to have a larger effect, especially on R_0A through the tunneling leakage current. The nonlinear dependence of the junction characteristics on dislocation density is examined, and is proposed as a natural explanation for the observed nonlinear behavior of R_0A .

REFERENCES

1. S.M. Johnson, R. Righer, J.P. Rosbeck, J.M. Peterson, S.M. Taylor, and M.E. Boyd, *J. Vac. Sci. Technol. B* **10**, 1499 (1992).
2. S.H. Shin, J.M. Arias, D.D. Edwall, M. Zandian, J.G. Pasko, and R.E. DeWames, *J. Vac. Sci. Technol. B* **10**, 1492 (1992).
3. K. Kosai and W.A. Radford, *J. Vac. Sci. Technol. A* **8**, 1252 (1990).
4. R.E. DeWames, private communication (1993).
5. P.I. Baranskii, A.E. Belyaev, O.P. Gorodnicheii, and S.M. Komirenko, *Sov. Phys. Semicond.* **24**, 73 (1990).
6. J.C. Zolper and A.M. Barnett, *IEEE Trans. Elect. Dev.* **37**, 478 (1990).
7. D. Gerthsen, F.A. Ponce, and G.B. Anderson, *Philosophical Magazine A* **59**, 1045 (1989).
8. G. Saada, *Phys. Stat. Sol. (B)* **44**, 717 (1971).
9. G. Faivre and G. Saada, *Phys. Stat. Sol. (B)* **52**, 127 (1972).
10. H. Booyens and J.S. Vermaak, *J. Appl. Phys.* **50**, 4302 (1979).
11. H. Booyens and J.H. Basson, *Phys. Stat. Sol. (A)* **85**, 243 (1984).
12. P. Fedders, *J. Appl. Phys.* **54**, 1804 (1983).

Appendix B

TRANSPORT STUDIES IN NARROW-GAP SEMICONDUCTORS REVISITED

TRANSPORT STUDIES IN NARROW-GAP SEMICONDUCTORS REVISITED

August 1993

Srinivasan Krishnamurthy and Arden Sher
SRI International, Menlo Park, CA 94025

ABSTRACT

Transport-related properties such as electron mobility, Hall coefficient, Fermi level, and energy gap are calculated with accurate analytical band structures and Fermi-Dirac statistics. Calculated values differ substantially from the ones obtained with effective mass or parabolic band structure approximation of $\text{Hg}_{0.22}\text{Cd}_{0.78}\text{Te}$ alloy.

1. INTRODUCTION

The experimental results on electron transport properties of semiconductors are often compared to theory that rests on three approximations, namely, parabolic band structures for those states occupied in the measurement, Maxwell-Boltzmann (MB) statistics, and collision time approximation to a full Boltzmann gain-loss equation. These approximations are made to all scattering mechanisms, whether they are elastic or inelastic. It is well known that, even in large-gap materials, the constant effective mass approximation is valid only very near ($\approx E_g/10$) to the band edge.^{1,2} This approximation has been recognized to be particularly poor for narrow-gap materials and nonparabolic corrections calculated in the $k \cdot p$ formalism.³⁻⁵ This correction is substantial, but still differs considerably from our more accurately calculated band structures. In addition, our fit of the conduction band to an analytical function makes many results

transparent and simplifies the calculations. As the Fermi energy can easily move into the conduction band of lightly doped small-gap materials, the form of the Boltzmann equation with Fermi-Dirac (instead of the usual MB) statistics must be used to obtain accurate transport coefficients.

We report results from our study of absorption coefficient, Fermi energy, Hall coefficient, and electron mobility calculated with Fermi-Dirac statistics (FD), and an accurate pseudopotential band structure fine-tuned with tight-binding (TB) corrections.

2. BAND STRUCTURE

Quantitatively accurate band structures of group IV elements,⁶ III-V compounds,⁷ and II-VI compounds^{7,8} can be obtained using a minimum set of sp^3 orbitals in semiempirical calculations. First, empirical pseudopotential form factors are used to calculate a TB Hamiltonian, H in the minimum set. H is then transformed into a zeroth order H_0 in an orthonormal basis. Then, a perturbative Hamiltonian having a first-neighbor TB form is added to H_0 to fine-tune the band structure. Because long-range interactions are included in this Hamiltonian, the measured band curvatures are correctly reproduced. This procedure is followed for both HgTe and CdTe, and then the alloy band structures are calculated in the coherent potential approximation.

We focus $Hg_{0.22}Cd_{0.78}Te$ alloy with 100-meV band gap for the studies reported here. We find that the calculated conduction band is replicated very well by a hyperbola,

$$E_k = (\gamma k^2 + c^2)^{1/2} - c \quad (1)$$

where γ and c are adjusted to fit the calculated band structure in the energy range of interest. When γ and c are treated as constants related to the band gap, E_g and the effective mass, this expression reduces to the same nonparabolic correction form obtained in the $k \cdot p$ method.⁴ However, the numerical value of γ and c are not same as ours. For example, in the chosen case, γ and c are 48.3 and 0.058 respectively, whereas the corresponding $k \cdot p$ values are 36.0 and 0.05. The differences are found to be large enough to cause a noticeable change in the band structure.

The band structure calculated by diagonalizing the Hamiltonian is shown in Figure 1 (thick, solid lines). We can see that the fitted band structure (thin line) agrees quite well up to an energy of 0.5 eV from the conduction band edge. Without loss of accuracy, in the studies considered here, Eq. 1 is used as the energy-dispersion relation in the transport expressions. Also shown in Figure 1 is the poor reproduction of the conduction band obtained with an effective mass approximation (dashed line).

Two qualitative features of the band structure in Figure 1 that impact transport properties should be noted. First, for energies $E - E_c$ greater than 50 meV where the shape of the conduction band is nearly linear in k , the group velocity is a constant independent of the k . Then, the density of states (DOS) increases proportional to E rather than $E^{1/2}$ as in the case of parabolic bands. Clearly, these features modify the transport properties of electrons occupying these states. As we will show in the following section, at the carrier concentration and temperatures often found in device structures, the Fermi level falls into the region where these features contribute.

3. FERMİ LEVEL

The calculation of Fermi level ϵ_F as a function temperature T and doping concentration n_D is required for all transport calculations. A knowledge of temperature-dependent gap $E_g(T)$ is essential to obtain ϵ_F . Ideally, temperature dependence should be included in the Hamiltonian from which the variation of E_g with T could be obtained. We have developed a general method to incorporate phonon and alloy effects into the same CPA formalism,⁹ but such an approach is not attempted here. Instead, we use the expression¹⁰ given by

$$E_g = 0.0954 + 0.0327 T/1000 \quad (2)$$

After studying the effects of various approximations and obtaining trends, the calculations is repeated with the temperature-dependent Hamiltonian.

Then, the ϵ_F is calculated from the condition¹¹ that at a given T the number of electrons in the conduction band is the sum of electrons excited from the valence band and donor levels.

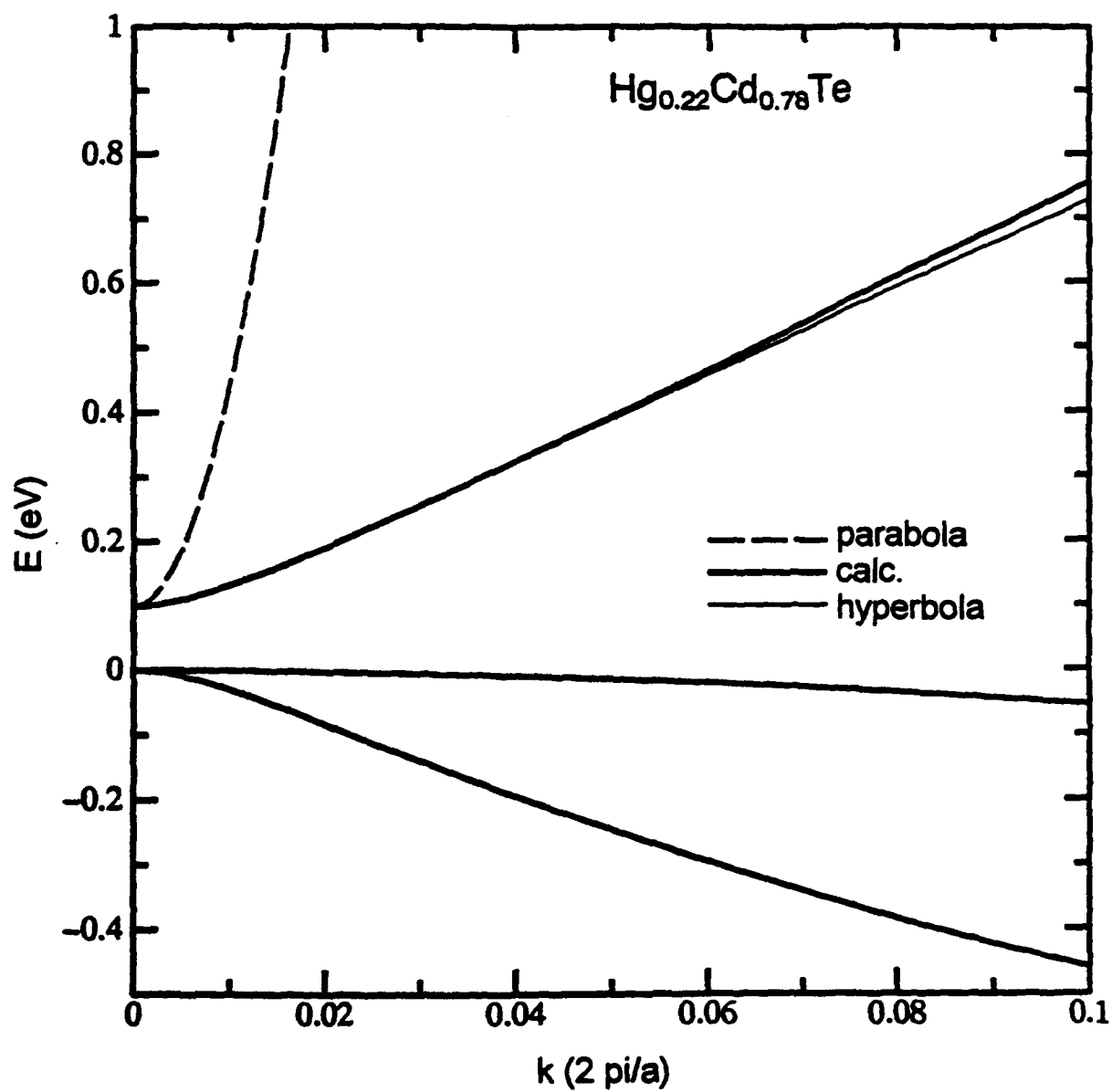


Figure 1. Electronic structure of HgCdTe

In this study where the modifications caused by the band structures are being emphasized, the donor states are assumed to be located at the bottom of the conduction band. The valence and conduction band DOS are calculated from our band structure. The valence band DOS yields a hole effective mass of 0.65. The ϵ_F (measured from valence band edge) as a function of T and n_D calculated from parabolic and hyperbolic band structures are given in Figure 2, a and b respectively. As expected, a hyperbolic band makes a substantial change from parabolic-band-generated values. The impact on the transport properties is large when ϵ_F is located at energy where the band changes its character from parabolic to linear. In addition, when ϵ_F is near to or greater than E_g , the absorption cutoff wavelength is strongly influenced. A proper account of the Moss-Bernstein shift must include these accurate band structures. We also note that the Fermi level and the measured band gap affect each other. Hence, a proper data reduction of cutoff wavelength determination of the energy gap has to be done self-consistently.

4. ENERGY GAP

To emphasize the point that the measured value of E_g and its T dependence is sensitively dependent on the knowledge of ϵ_F , we carried out a calculation of absorption coefficient α . The absorption coefficient α is proportional to $k^2 \rho_c (1 - f_c) \rho_v f_v$, where f is the FD distribution function, ρ is the DOS, and subscripts c, v represent conduction and valence band, respectively. The k^2 factor arises from the matrix elements that are in the expression for ϵ_F . The temperature- and energy-independent proportionality constant is adjusted to agree with the experimental curve at 80 K in the vicinity of a given value of α . Nearly linear dependence of $\ln(\alpha)$ on photon energy was observed¹² for T between 80 and 300 K and Hg concentrations near 0.22.

Because the band edges are broadened by impurity and phonon scattering (Urbach tail or broadening), the gap cannot simply be assigned to the energy wave length where these curves project to zero. The procedure used by many authors is to assign λ_{co} to be the place where α is 500 cm^{-1} or 1000 cm^{-1} . In the spirit of this procedure, we adjust our proportionality constant to fit the $\ln(\alpha)$ versus E curve at 80 K. As seen from Figure 3a, one constant fits the entire curve.

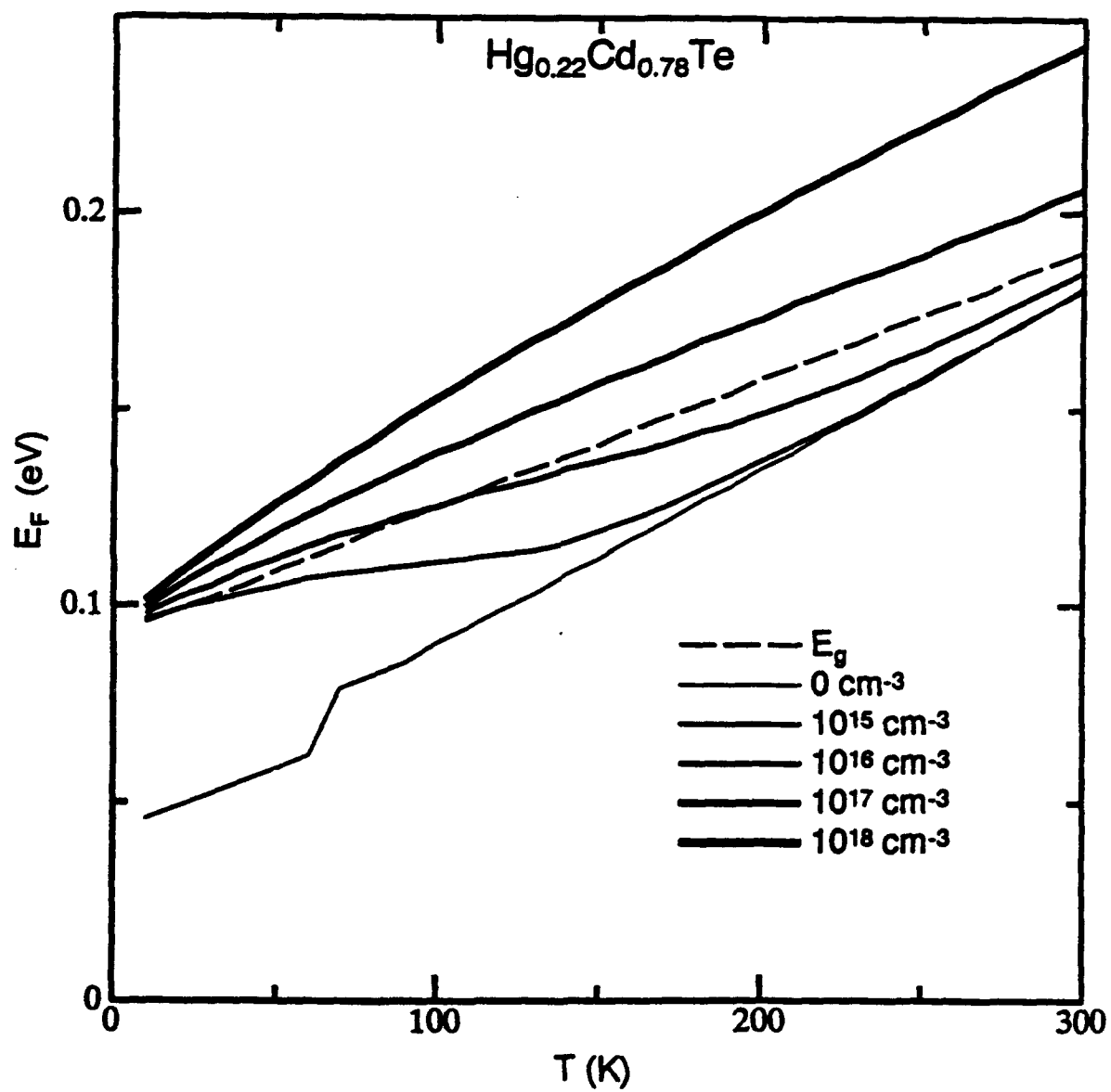


Figure 2a. Fermi energy as a function of temperature: parabolic bands

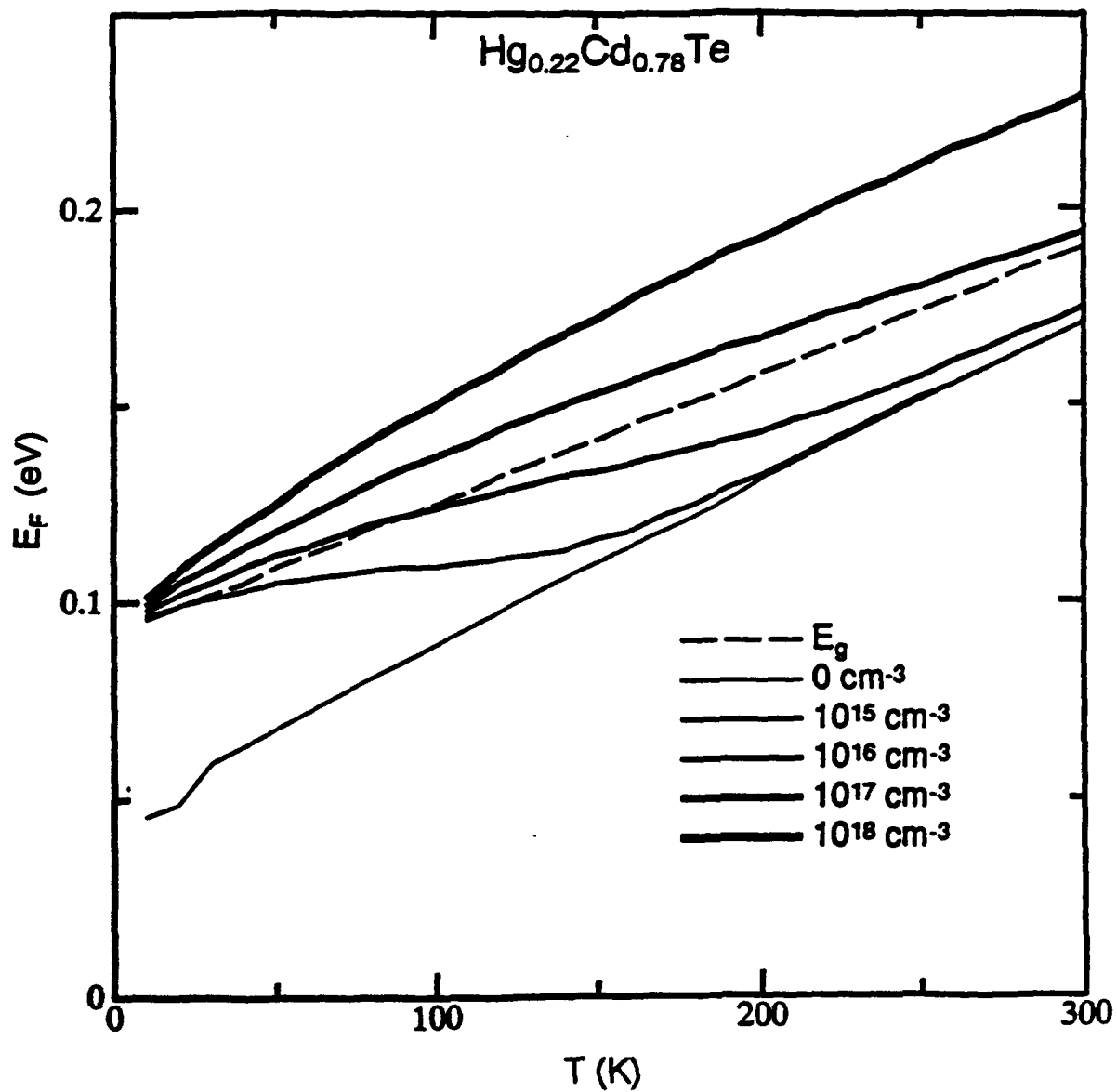


Figure 2b. Fermi energy as a function of temperature: hyperbolic bands

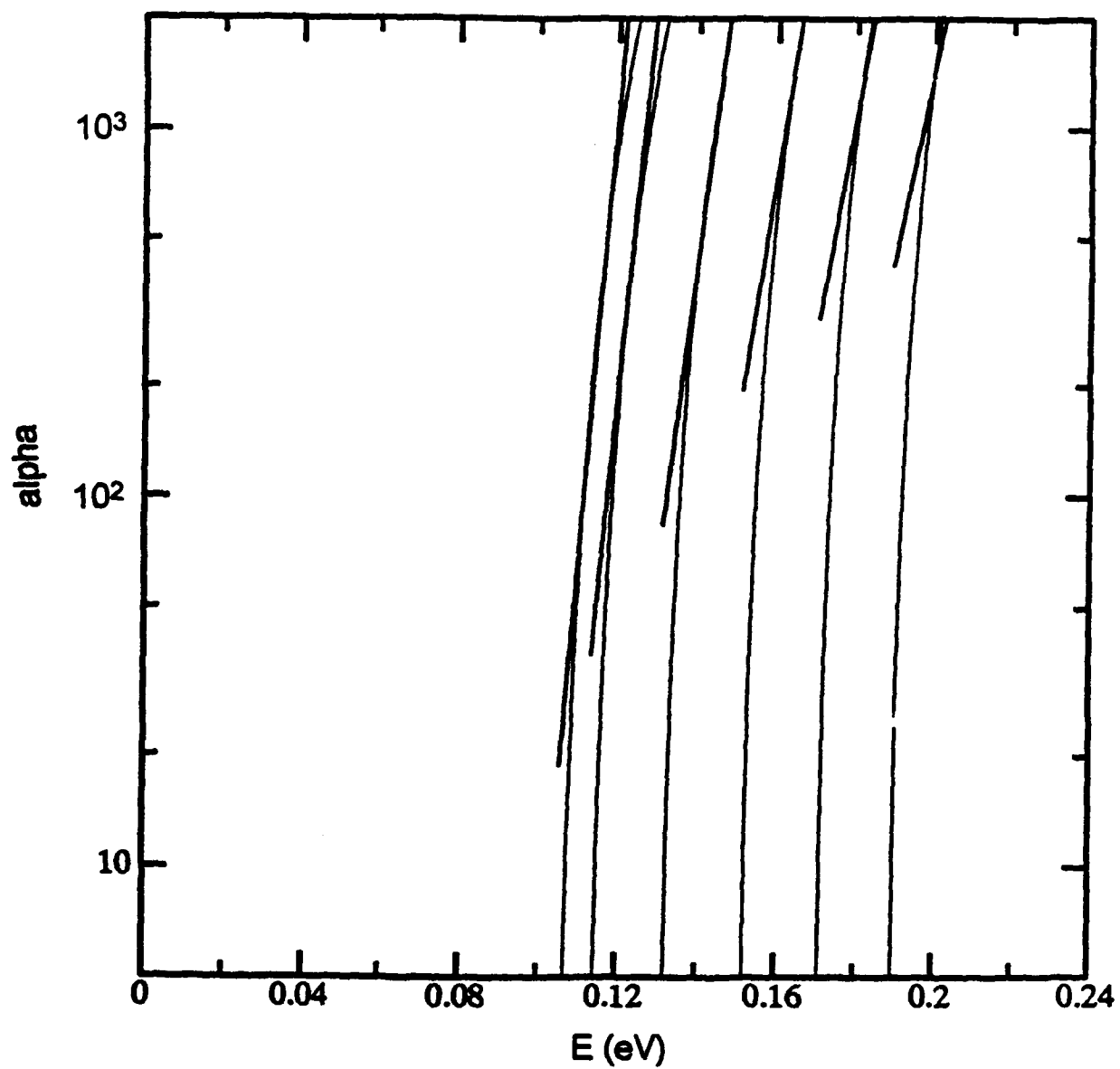


Figure 3a. Absorption coefficient as a function of photon energy

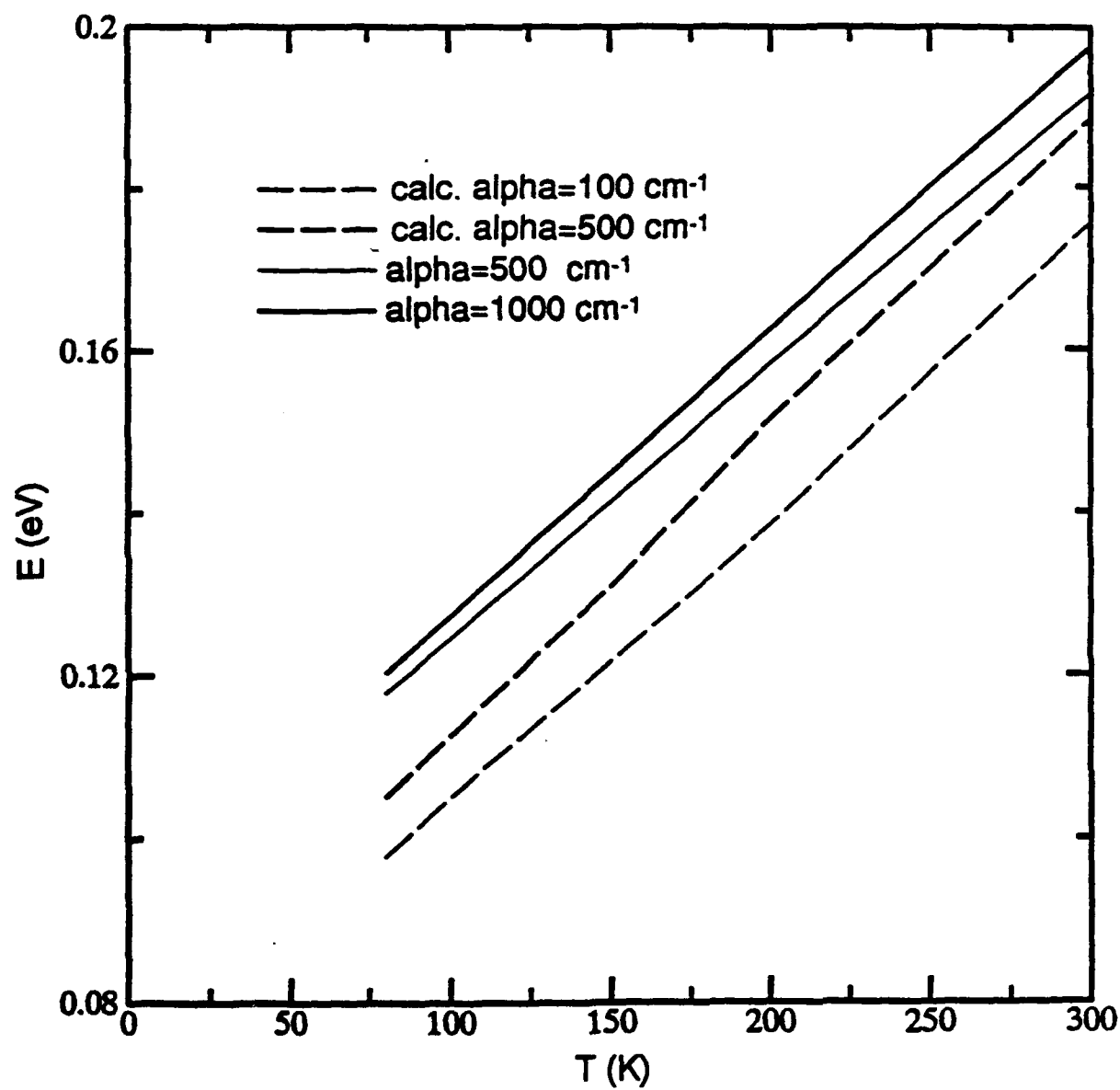


Figure 3b. Energy gap as a function of temperature

However, at higher temperatures the tail sets. We then recalculate the band structures and α for different band gaps (with corresponding curvature) until the curves at $\alpha = 500 \text{ cm}^{-1}$ for all temperatures, as shown in Figure 3a. The energy gap, variation with temperature, deduced by following this procedure is shown in Figure 3b (a dashed line). Also shown in Figure 3b (solid lines) for comparison are effective E_g versus T variations if values are taken from the data corresponding to $\alpha = 500 \text{ cm}^{-1}$ and 1000 cm^{-1} . Finally, because our procedure is ad hoc, we repeated our fits by adjusting to $\alpha = 100 \text{ cm}^{-1}$ values; the calculated energy gaps are also plotted in Figure 3b (a dashed line). We expect that the proper $E_g(T)$ curve lies somewhere between our two fit curves. Note that both curves are below the traditional curves and the variation in T is no longer linear, emphasizing the need for proper calculation of $E_g(T)$, $\alpha(T)$ so that more reliable device parameters can be established.

5. HALL COEFFICIENT

The carrier density, n in n -type material, is normally deduced from measurements of the Hall coefficient R_H , given by r_e/en , by assuming the Hall factor r_e is unity. If one uses parabolic approximation and MB statistics, r_e is approximately unity. We set out to examine the effect of removing these approximations, using the correct band structures. This requires generalizing the Boltzmann transport equation (BTE) to include the FD distribution function. We have

$$\frac{df(\mathbf{k})}{dt} = \sum_{\mathbf{k}'} [w(\mathbf{k}, \mathbf{k}')f(\mathbf{k}')(1-f(\mathbf{k})) - w(\mathbf{k}', \mathbf{k})f(\mathbf{k})(1-f(\mathbf{k}'))] \quad (3)$$

The first term of the right side of Eq. 3 is the gain term, and the second one is the loss term. In equilibrium, the left side of Eq. 3 is identically zero, and f becomes the equilibrium FD distribution function f_0 given by

$$f_0(E_k) = (e^{\beta(E_k - \epsilon_F)} + 1)^{-1} \quad (4)$$

where β is $(k_B T)^{-1}$. In the presence of the electric and magnetic field

$$\frac{df(k)}{dt} = \frac{\partial f(k)}{\partial t} + \nabla f(k) \cdot \frac{e}{\hbar} (E + v \times B) \quad (5)$$

In steady state, the $\partial f(k)/\partial t$ in Eq. 5 vanishes. In the small-field regime, we can linearize f and write it as a sum of f_0 and a perturbation $f_1(k)$. Disregarding the derivative of $f_1(k)$ and after some algebraic manipulation, Eq. 5 reduces to

$$\nabla f_0(k) \cdot \frac{e}{\hbar} (E + v \times B) = \sum_{k'} [W(k, k') f_1(k') - W(k', k) f_1(k)] \quad (6)$$

where the renormalized W and the usual transition probability per unit time w are related by

$$W(k, k') = w(k, k') \frac{(1-f_0(k))}{(1-f_0(k'))} \quad (7)$$

Note that for elastic scattering W and w are equal. However, for inelastic cases the effect depends on whether energies at k and k' are larger or smaller than ϵ_F . If both initial and final energies are larger (or smaller) than ϵ_F , only small correction to w is expected. However, if the initial state is above ϵ_F and the final state is below ϵ_F , that scattering is suppressed.

In the collision time approximation, the gain term in Eq. 7 is neglected and the effective collision time τ_k^F is

$$(\tau_k^F)^{-1} = \sum_{k'} W(k', k) \quad (8)$$

Using this collision time approximation, it is straightforward to obtain the expression for r_e :

$$r_e = 3k_B T \left[\frac{\sum_k f_0 \sum_k k^2 \gamma_k^3 (\tau_k^F)^2 f_0 (1-f_0)}{(\sum_k k^2 \gamma_k^2 (\tau_k^F)^2 f_0 (1-f_0))^2} \right] \quad (9)$$

where $\nabla_k E_k$ is $\gamma_k k$. The calculated r_e with parabolic and hyperbolic band structures is shown for various T and doping densities in Figure 4, a and b respectively. In both cases, the r_e is approximately 1 for higher temperatures. At lower temperatures, it shows considerable structure with a maximum value of about 2 obtained in parabolic approximation. However, when more accurate hyperbolic band structure is used, the variation with T is reduced to a maximum value of about 1.2, suggesting that reported intrinsic densities may be smaller by approximately 20%. The effect of collision time approximation and T dependence of band gap on the values of r_e still

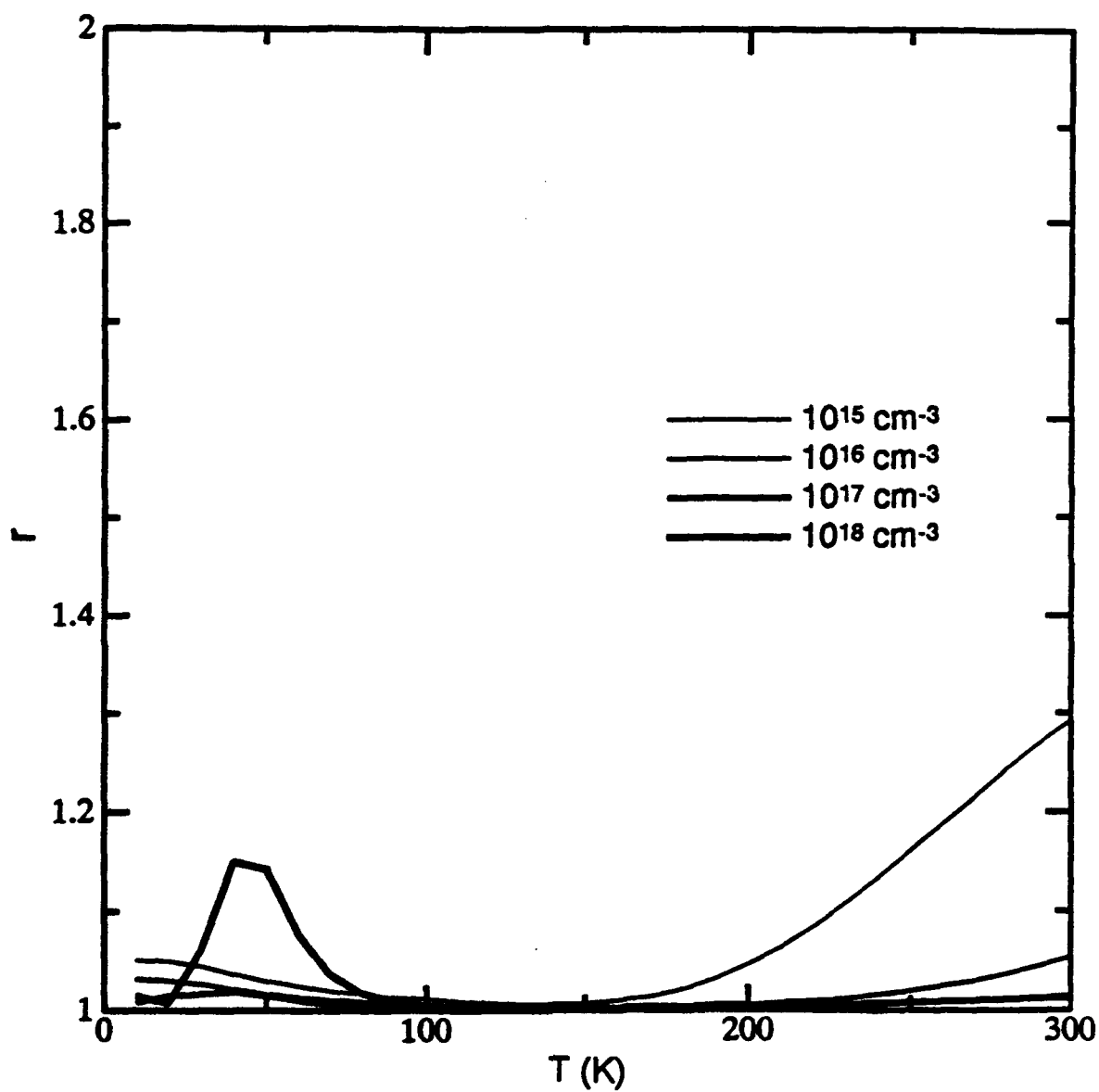


Figure 4a. Hall factor as a function of temperature: hyperbolic bands

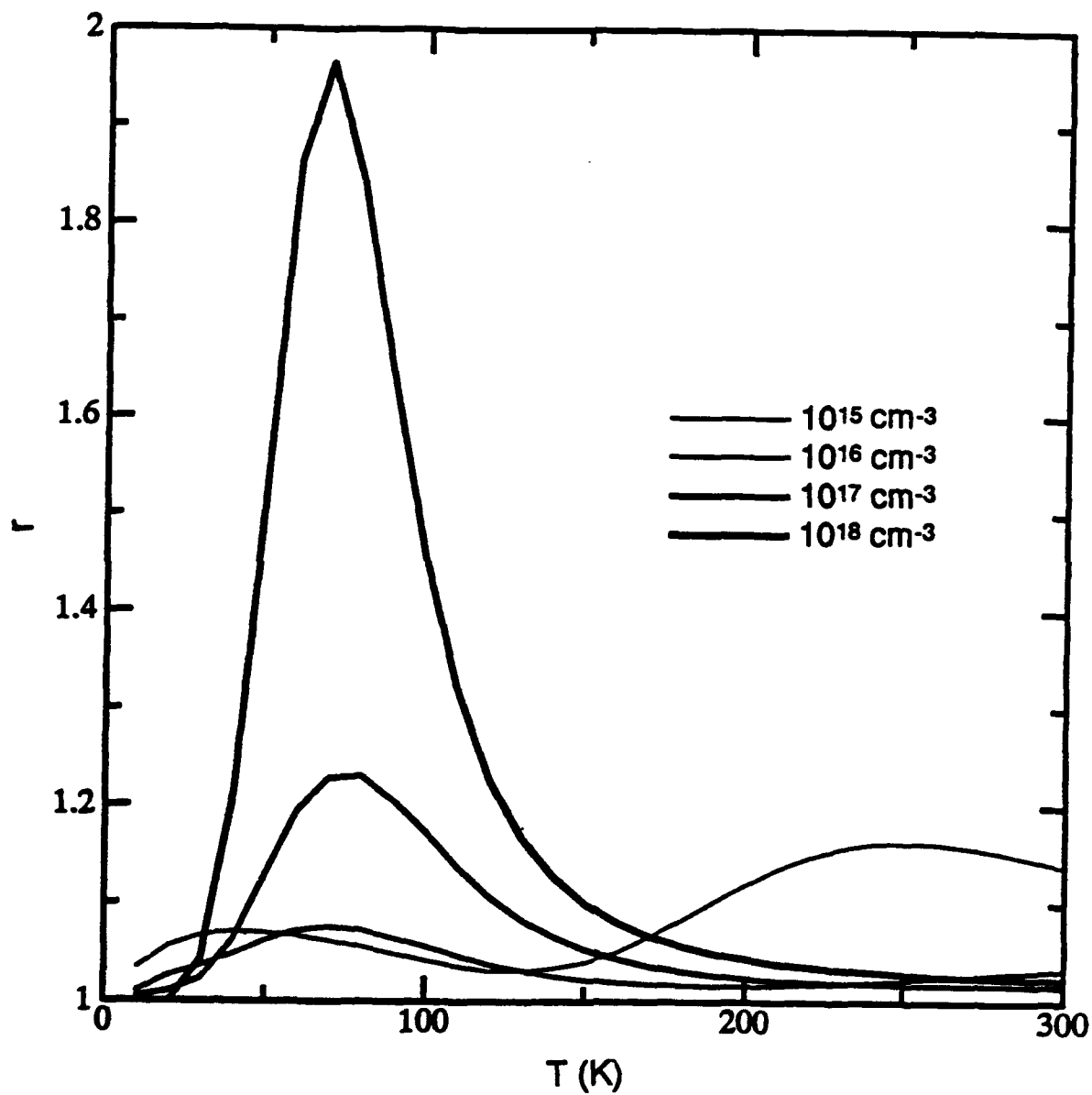


Figure 4b. Hall factor as a function of temperature: parabolic bands

need to be studied to extract correct carrier densities from Hall measurements. However, our tentative conclusion is that approximating r_e to be 1 is better than we had expected.

6. DRIFT MOBILITY

The formalism developed above to find a solution to BTE with FD statistics can be used to calculate the mobility, μ . We obtain the following expression in collision time approximation:

$$\mu = \frac{e}{3\hbar^2 k_B T} \left[\frac{\sum_{\mathbf{k}} k^2 \gamma_{\mathbf{k}}^2 \tau_{\mathbf{k}}^F f_0(1-f_0)}{\sum_{\mathbf{k}} f_0} \right] \quad (10)$$

The mobility calculated by including the scattering due to ionized impurities and polar optic phonons as a function of temperature and doping density is shown in Figure 5a. The change in the Debye screening length, complicated variation of Fermi level, and phonon scattering give rise to a crossover in mobility near 40 K, as seen in Figure 5a. However, it is well known that the collision time approximation always overestimates the velocity transition rate that determines the mobility.

For meaningful comparison with experiment, we generalized the above procedure to get full solution to BTE.¹³ Thus, calculated mobility with our hyperbolic band structure, and usual $\mathbf{k} \cdot \mathbf{p}$ band structure is shown along with that obtained in collision time approximation and compared with experiments¹⁴ in Figure 5b.

One important feature of Figure 5b is that the hump in mobility near 40 K could be explained with competing impurity and phonon scattering rates. Also note that collision time approximation grossly underestimates the mobility. Although $\mathbf{k} \cdot \mathbf{p}$ values are closer to experiment, the agreement is expected to be poor once the scattering mechanisms such as acoustic and alloy disorder and the effect of temperature-dependent band structures are included. These mechanisms lower the mobility calculated with hyperbolic band structures and yield an excellent agreement with experiment.

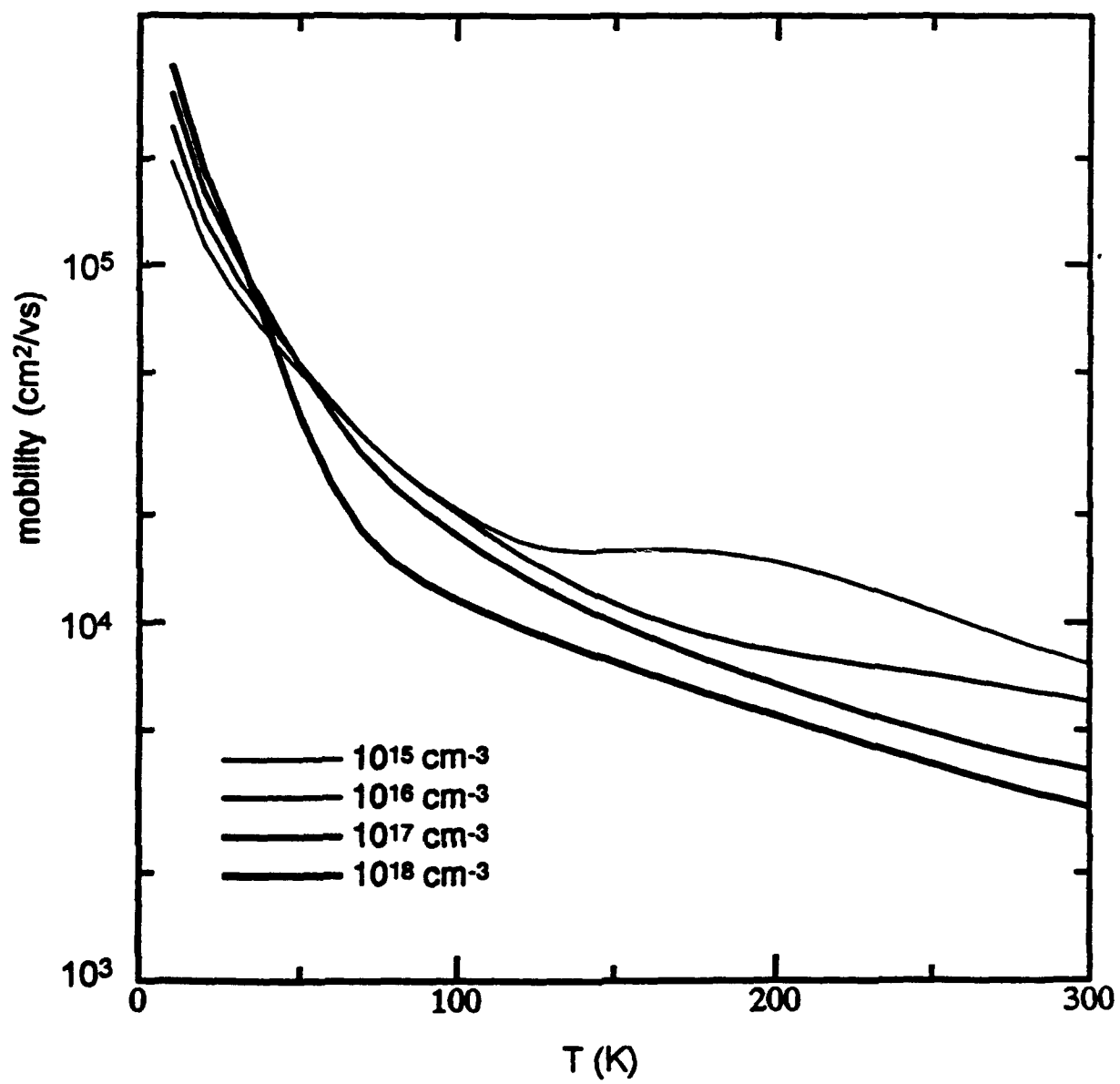


Figure 5a. Mobility with hyperbolic bands

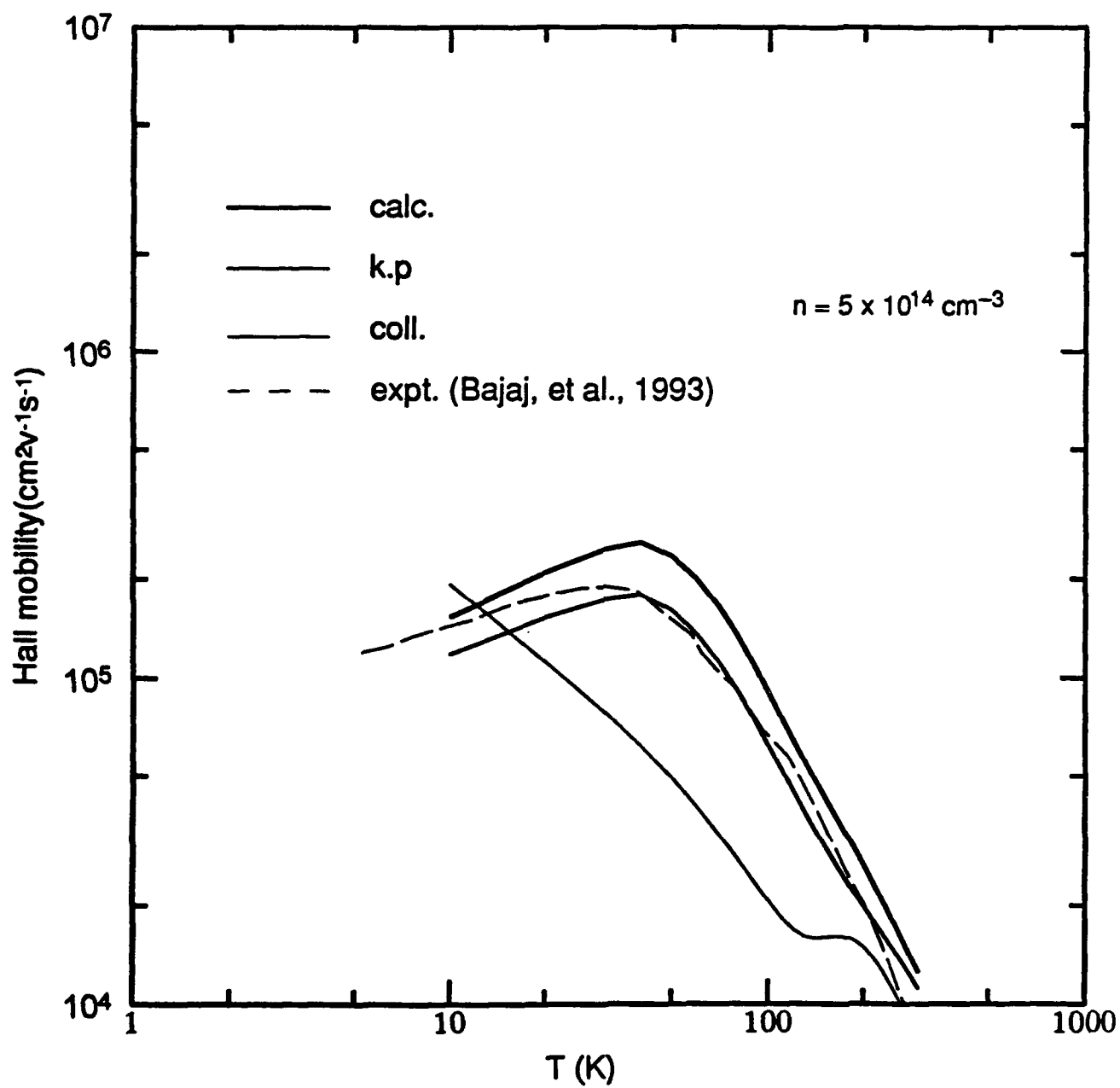


Figure 5b. Variation of Hall mobility with temperature

7. CONCLUSIONS

We have studied the effect of various approximations on electron transport coefficients and on ways to extract physical parameters from experiments. We point out how the values interpreted from experiments depend crucially on various approximations such as effective mass, MB statistics, and collision time. The results are

- Approximating the Hall factor by unity over a wide range of carrier concentrations and temperatures is accurate for most applications. An error of about 30% is expected at high temperatures and low carrier concentration (10^{14} cm^{-3}), and about 20% is expected at low T and high carrier concentration (10^{18} cm^{-3}).
- The variation of band gap with temperature is nonlinear and is faster at low temperature. The value at 22% Hg concentration is about 20 meV smaller than values usually quoted.
- The mobility calculated from full solution to BTE with FD statistics can explain the hump near 40 K and is in good agreement with experiments. Once the other scattering mechanisms such as acoustic and alloy disorder are included, the agreement is expected to be much better.

ACKNOWLEDGMENT

We thank Martha Berding for many valuable discussions and Dr. J. Bajaj for providing experimental mobility data. The work was supported in part by ARPA contract MDA972-92-C-0053 and ONR contract N00014-93-0091.

REFERENCES

1. Kane, E.O, 1957: J. Phys. Chem. Solids, **1**, 249.
2. Krishnamurthy, S., A. Sher, and A.-B. Chen, 1987: J. Appl. Phys., **61**, 1475.
3. Schmidt, J.L., 1970: J. Appl. Phys., **41**, 2876.
4. Meyer, J.R., and F.J. Bartoli, 1982: J. Vac. Sci. Technol., **21**, 237.
5. Bartoli, F.J., J.R. Meyer, R.E. Allen, and C.A. Hoffman, 1982: J. Vac. Sci. Technol., **21**, 241.
6. Krishnamurthy, S., A. Sher, and A.-B. Chen, 1986: Phys. Rev. B **33**, 1026.
7. Chen, A.-B., and A. Sher, 1981: Phys. Rev. B **23**, 5360.
8. Berding, M.A., S. Krishnamurthy, A. Sher, and A.-B. Chen, 1987: J. Vac. Sci. Technol., **A 5**, 3014.
9. Chen, A.-B., and A. Sher, 1972: Phys. Rev. B **5**, 2897.
10. Brice, J.C., 1986: *Properties of HgCdTe*, EMIS Datareview Series, No. 3, p. 103.
11. Sze, S.M., 1981: *Physics of semiconductor devices* (Wiley, New York), p. 22.
12. Finkman, E., and Y. Nemirovsky, 1979: J. Appl. Phys., **50**, 4356.
13. Krishnamurthy, S., and A. Sher 1993: The U.S Workshop on the Physics and Chemistry of HgCdTe and other IR materials, Seattle, Oct. 19-21.
14. Bajaj, J., S.H. Shin, G. Bostrup, and D.T. Cheung, 1982: J. Vac. Sci. Technol., **21**, 244; 1993, private communication.